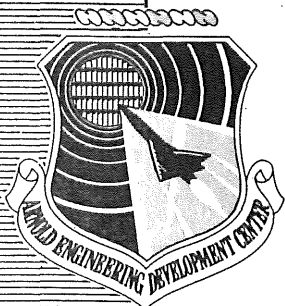


OCT 23 1975

NOV 12 1975

*copy 2*



# **PRESSURE AND HEAT-TRANSFER TESTS ON THE NASA SPACE SHUTTLE EXTERNAL TANK AT MACH NUMBER 16**

**VON KÁRMÁN GAS DYNAMICS FACILITY  
ARNOLD ENGINEERING DEVELOPMENT CENTER  
AIR FORCE SYSTEMS COMMAND  
ARNOLD AIR FORCE STATION, TENNESSEE 37389**

October 1975

Final Report for Period 9 August — 20 September, 1974

Approved for public release; distribution unlimited.

Property of U. S. Air Force  
AEDC LIBRARY  
F40600-75-C-0001

Prepared for

**NATIONAL AERONAUTICS AND SPACE ADMINISTRATION  
GEORGE C. MARSHALL SPACE FLIGHT CENTER  
MARSHALL SPACE FLIGHT CENTER, ALABAMA 35812**

## NOTICES

When U. S. Government drawings specifications, or other data are used for any purpose other than a definitely related Government procurement operation, the Government thereby incurs no responsibility nor any obligation whatsoever, and the fact that the Government may have formulated, furnished, or in any way supplied the said drawings, specifications, or other data, is not to be regarded by implication or otherwise, or in any manner licensing the holder or any other person or corporation, or conveying any rights or permission to manufacture, use, or sell any patented invention that may in any way be related thereto.

Qualified users may obtain copies of this report from the Defense Documentation Center.

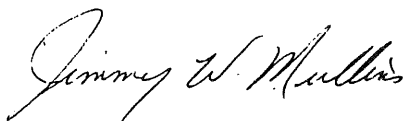
References to named commercial products in this report are not to be considered in any sense as an endorsement of the product by the United States Air Force or the Government.

This report has been reviewed by the Information Office (OI) and is releasable to the National Technical Information Service (NTIS). At NTIS, it will be available to the general public, including foreign nations.

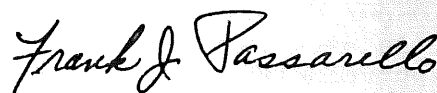
## APPROVAL STATEMENT

This technical report has been reviewed and is approved for publication.

FOR THE COMMANDER



JIMMY W. MULLINS  
Lt Colonel, USAF  
Chief Air Force Test Director, VKF  
Directorate of Test



FRANK J. PASSARELLO  
Colonel, USAF  
Director of Test

# UNCLASSIFIED

REPORT DOCUMENTATION PAGE		READ INSTRUCTIONS BEFORE COMPLETING FORM
1. REPORT NUMBER <b>AEDC-TR-75-31</b>	2. GOVT ACCESSION NO.	3. RECIPIENT'S CATALOG NUMBER
4. TITLE (and Subtitle) <b>PRESSURE AND HEAT TRANSFER TESTS ON THE NASA SPACE SHUTTLE EXTERNAL TANK AT MACH NUMBER 16</b>	5. TYPE OF REPORT & PERIOD COVERED <b>Final Report, 9 Aug - 20 Sept, 1974</b>	
	6. PERFORMING ORG. REPORT NUMBER	
7. AUTHOR(s) <b>L. G. Siler and A. H. Boudreau, ARO, Inc.</b>		8. CONTRACT OR GRANT NUMBER(s)
9. PERFORMING ORGANIZATION NAME AND ADDRESS <b>Arnold Engineering Development Center (XO) Arnold Air Force Station, TN 37389</b>		10. PROGRAM ELEMENT, PROJECT, TASK AREA & WORK UNIT NUMBERS <b>Program Element 921E2</b>
11. CONTROLLING OFFICE NAME AND ADDRESS <b>NASA-MSFC (A&amp;E-AERO-AT) Marshall Space Flight Center Alabama 35812</b>		12. REPORT DATE <b>October 1975</b>
14. MONITORING AGENCY NAME & ADDRESS (if different from Controlling Office)		13. NUMBER OF PAGES <b>48</b>
		15. SECURITY CLASS. (of this report) <b>UNCLASSIFIED</b>
16. DISTRIBUTION STATEMENT (of this Report)  <b>Approved for public release; distribution unlimited.</b>		15a. DECLASSIFICATION/DOWNGRADING SCHEDULE <b>N/A</b>
17. DISTRIBUTION STATEMENT (of the abstract entered in Block 20, if different from Report)		
18. SUPPLEMENTARY NOTES  <b>Available in DDC.</b>		
19. KEY WORDS (Continue on reverse side if necessary and identify by block number) <div style="display: flex; justify-content: space-between;"> <div> space shuttles fuel tanks distribution pressure </div> <div> wind tunnel tests test method heat transfer rate </div> </div>		
20. ABSTRACT (Continue on reverse side if necessary and identify by block number) <p>An experimental test program was conducted in the AEDC-VKF Hypervelocity Wind Tunnel (F) at a nominal Mach number of 16 to obtain basic heating and pressure distribution data on the NASA Space Shuttle external tank. The tests were conducted over an attitude range which simulated tank tumbling after separation from the Shuttle orbiter. The angles of attack varied from 0 to -180 deg with combinations of roll from 0 to 90 deg at free-stream</p>		

# UNCLASSIFIED

UNCLASSIFIED

20, Continued

Reynolds numbers (based on model length) from  $0.38 \times 10^6$  to  $1.10 \times 10^6$ . In addition to surface heat-transfer gages, thermographic phosphor paint was used to determine the interference heating factors on and around the various attachment structures and service ducts.

UNCLASSIFIED

## PREFACE

The work reported herein was conducted by the Arnold Engineering Development Center (AEDC), Air Force Systems Command (AFSC), at the request of the National Aeronautics and Space Administration, Marshall Space Flight Center, under Program Element 921E-2. The results of the test were obtained by ARO, Inc. (a subsidiary of Sverdrup & Parcel and Associates, Inc.), contract operator of AEDC, AFSC, Arnold Air Force Station, Tennessee, under ARO Project No. V41F-25A. The authors of this report were L. G. Siler and A. H. Boudreau, ARO, Inc. The data analysis was completed October 23, 1974, and the manuscript (ARO Control No. ARO-VKF-TR-74-129) was submitted for publication on December 20, 1974.

## CONTENTS

	<u>Page</u>
1.0 INTRODUCTION . . . . .	5
2.0 APPARATUS	
2.1 Tunnel and Nozzle Description . . . . .	5
2.2 Model . . . . .	6
2.3 Instrumentation . . . . .	6
3.0 PROCEDURE	
3.1 Test Procedures . . . . .	8
3.2 Test Conditions . . . . .	9
3.3 Data Acquisition . . . . .	9
3.4 Data Precision . . . . .	10
4.0 RESULTS AND DISCUSSION . . . . .	11
5.0 CONCLUSIONS . . . . .	14
REFERENCES . . . . .	15

## ILLUSTRATIONS

### Figure

1. Typical External Tank Entry Trajectory Compared with Tunnel F Test Condition . . . . .	17
2. Photograph of the NASA External Tank 0.015-Scale Model . . . . .	18
3. Sketch Illustrating Model and Sting Details . . . . .	19
4. NASA External Tank (0.015-Scale Model) Installation in Tunnel F . . . . .	20
5. Sketch Illustrating Pressure and Heat-Transfer Gage Locations . . . . .	21
6. Typical Analog Data Traces and Variation of Test Conditions . . . . .	22
7. Typical Phosphor Paint Results, $\alpha' = -30$ deg, $\phi' = 0$ . . . . .	23
8. External Tank Windward Centerline ( $\theta = 0$ ) Heat-Transfer and Pressure Distributions . . . . .	28
9. Variation of External Tank Heat-Transfer and Pressure Distributions on Model Centerline ( $\theta = 0$ ) with Roll Angle . . . . .	30
10. External Tank Peripheral Heat-Transfer and Pressure Distributions for $\alpha' = 0$ . . . . .	33
11. External Tank Peripheral Heat-Transfer and Pressure Distributions for $\alpha' = -30$ deg . . . . .	34
12. External Tank Peripheral Heat-Transfer and Pressure Distributions for $\alpha' = -60$ deg . . . . .	36

<u>Figure</u>	<u>Page</u>
13. External Tank Peripheral Heat-Transfer and Pressure Distributions for $\alpha' = -90$ deg . . . . .	38
14. Heat-Transfer and Pressure Peripheral Distributions Normalized to Stagnation Line Values for $\alpha' = -30, -60$ , and $-90$ deg at $x/\ell = 0.35$ . . . . .	41

### TABLES

1. Gage Locations . . . . .	42
2. Summary of Model Instrumentation . . . . .	43
3. Test Summary . . . . .	45
4. Summary of Tunnel Conditions . . . . .	46

NOMENCLATURE . . . . .	47
------------------------	----

## 1.0 INTRODUCTION

The National Aeronautics and Space Administration/Marshall Space Flight Center (NASA/MSFC) External Tank Heat Test (TH1F) was a program designed to obtain basic heat and pressure distribution data on a 0.015-scale model of the Space Shuttle external tank. The tests were conducted in the AEDC von Kármán Gas Dynamics Facility (VKF) Hypervelocity Wind Tunnel (F).

A typical external tank entry trajectory is shown in Fig. 1. The high altitude-high Mach number regime (altitude  $> 250,000$  ft and  $M_\infty > 24$ ) was the region of interest. In order to simulate the Reynolds number corresponding to  $h = 250,000$  ft, it was necessary to conduct the test at Mach number 16. The objectives of this test were to define the surface pressure and heat-transfer-rate distributions and to obtain the interference heating levels on and around the various protuberances at a nominal Mach number of 16 for various combinations of angle of attack and roll. The tests were conducted over a Reynolds number range from  $0.38 \times 10^6$  to  $1.10 \times 10^6$ , based on model length.

## 2.0 APPARATUS

### 2.1 TUNNEL AND NOZZLE DESCRIPTION

Tunnel F is an arc-driven wind tunnel of the hotshot type (Ref. 1) and capable of providing Mach numbers from about 7.5 to 20 over a Reynolds number per ft range from  $0.05 \times 10^6$  to  $70 \times 10^6$ . Test sections of 108-in. diameter ( $M_\infty = 14$  to 20) and 54-in. diameter ( $M_\infty = 10$  to 17) are available using a 4-deg, half-angle conical nozzle. The range of Mach numbers at a particular test section in the conical nozzle is obtained by using various throat diameters. Two axisymmetric contoured nozzles ( $M_\infty = 8$  and 12) having exit diameters of 25 and 40 in., respectively, and which connect to the 54-in.-diam test station are also available. The test gas can be either air or nitrogen. The test gas for aerodynamic and aerothermodynamic testing is nitrogen. Air is used for combustion tests. The test gas is confined in either a 1.0-, a 2.5-, or a 4.0-ft<sup>3</sup> arc chamber, where it is heated and compressed by an electric arc discharge. The increase in pressure results in a diaphragm rupture with the subsequent flow expansion through the nozzle. Test times are typically from 50 to 200 msec. Shadowgraph and schlieren coverage are available at both test sections.

This test was conducted in the 108-in.-diam test section of the conical nozzle for  $M_\infty = 16$ . Nitrogen was the test gas. The 2.5-ft<sup>3</sup> volume arc chamber was used, and useful test times up to approximately 50 msec were obtained. Because of the relatively short test times, the model wall temperature remained essentially invariant from the initial value of approximately 540°R.



## 2.2 MODEL

The model was a 0.015-scale model of the NASA Shuttle external tank. The full-scale tank had a reference length of 1814.88 in. and a diameter of 330 in., which produced a model reference length of 27.223 in. and a model diameter of 4.95 in. The tank was basically an ogive cylinder with an elliptical base and a hemisphere cylinder nose vent cap, as is shown in Figs. 2 and 3. It was equipped with various external fuel lines, service pipes, wire tunnels, and the necessary structures for mating with the orbiter model. The model, designed and fabricated by NASA/MSFC, was machined of stainless steel and was made in several sections to facilitate gage installation and repair. The Martin Marietta Drawing No. 82600205022 was used for the basic tank and protuberance dimensions.

Because the angle-of-attack and roll requirements were outside the capability of the Tunnel F standard model support system, an attitude mechanism was incorporated into the model-sting design. There were three separate model-stings used during the test - one of which is shown in Figs. 2 and 3. With this sting the angle of attack could be varied from 0 to -90 deg in increments of 30 deg. To obtain greater angles of attack the model was rotated 180 deg in the horizontal plane and then reattached to the model-sting so that the same mechanism provided -90 to -180 deg angles of attack, in increments of 30 deg. A second model-sting of similar design, but with the model attachment pad rotated 90 deg in the horizontal plane, was used for runs where an angle of attack of -90 deg was desired along with the capability of rolling the model about its longitudinal axis. The third model-sting incorporated a continuously variable pitch and yaw arrangement which had the capability of attaining  $\alpha_s \leq 60$  deg simultaneously with  $\psi_s \leq 60$  deg. The model attitude was defined using a pitch-yaw-roll sequence.

The model-sting attached to the model at one of three possible locations. These locations are indicated in Figs. 3 and 4 and were chosen so that the sting would be as remote as possible from the upstream end of the model and also maintain the model within the tunnel window area for all model positions. A typical NASA/MSFC external tank installation in Tunnel F is shown in Fig. 4.

## 2.3 INSTRUMENTATION

The model, shown in Fig. 5, was instrumented with an array of pressure and heat-transfer-rate gages. Measurements were made at 62 locations. Eighteen of these were surface pressure ports, and the remainder were heat-transfer-rate gage locations. Thirty-three gages were located peripherally at several axial locations. Table 1 gives the axial and peripheral location of each gage.

Due to the broad test matrix the surface pressure and heat-transfer rate measurements varied over an extensive range between runs and locations on the model. The model was instrumented such that particular types of gages were used at specific locations to cover the range of measurements anticipated. Table 2 indicates the type of gage used at each location for each run, the normal measurement range of each gage, and, in the case of heat gages, whether a preamplifier was used in the measurement circuit. These variables were used in determining the uncertainty levels indicated in Tables 2c and d.

The surface pressure gages were of two types. Strain-gage-type transducers with a design range of 0.01 to 2.0 psid were used during the first twelve runs for all surface pressure measurements. Variable reluctance transducers with a design range from 0.001 to 0.1 psid were substituted for several of the strain-gage transducers in the most leeward locations during the pitch-roll series of runs. The model was reinstrumented prior to run 4874 in anticipation of lower overall surface pressure measurements where the variable reluctance gage became the primary gage. The variable reluctance gage was used on the cylinder section of the model and in a staggered arrangement with the strain-gage transducer on the ogive nose section. The staggered arrangement was designed to eliminate the need for changing gages during the final ten-run series, which included runs at angles of attack of 0 and -180 deg.

The surface heat-transfer-rate gages were also of two types. During the first 23 runs the primary gage was the coaxial surface thermocouple gage developed at AEDC-VKF. The basic thermocouple assembly consists of an electrically insulated Chromel<sup>®</sup> center conductor enclosed within a concentric cylindrical jacket of constantan. The thermocouple junction is formed at one end of the assembly by a mechanical abrasion technique. The thermocouple assemblies are small, typically 0.065 to 0.125 outside diameters, and are mounted with the thermocouple junction flush with the model surface. The coaxial type of gage was used primarily on the windward surfaces. However, as the test progressed, many of these gages became leeward gages, depending on the angle of attack and roll. To increase their output signals, preamplifiers were used in their circuits. The gages which had preamplifiers are indicated in Table 2.

The slug calorimeter (RT) type of heat gage was used in the regions where the lowest heat-transfer-rate measurements were anticipated. Slug calorimeters have a thin-film platinum resistance thermometer to sense the temperature of an aluminum disk which is exposed to the heat flux to be measured. The calorimeters are optimized to measure a given range of heat transfer by appropriate selection of the aluminum disk thickness. In the first 23 runs this type of gage was used for the leeward gages. However, for the final ten runs the slug calorimeter was the primary type of heat gage and was used at 37 of the 44 gage locations.

To monitor the tunnel conditions, two 1.0-in.-diam hemisphere-cylinders instrumented with slug calorimeter-type heat gages were installed in the test section to determine the stagnation heat-transfer rate (see Fig. 4). A pitot probe located near the heat probes measured the test section pitot pressure. Both the pitot and tunnel reservoir pressures were measured with strain-gage-type transducers developed at AEDC-VKF. Detailed information concerning heat-transfer and pressure instrumentation used can be found in Refs. 1, 2, and 3.

On selected runs (see Table 3), thermographic phosphor paint was used in conjunction with model heat-transfer-rate gages to obtain model heat flux distributions. Two types of phosphor paint were used to obtain heat-transfer-rate data during the course of the test. Radelin<sup>®</sup> phosphor 1807 was used at wall temperatures below 150°F, and phosphor 3251 was used at wall temperatures from 150 to 350°F. The phosphors were mixed with cellulose acetate buterate dope and sprayed on the model surface in thicknesses of 0.003 to 0.005 in.

The thermographic phosphor paint technique works on the principle of phosphorescence, which is the emission of luminescent light. This process is temperature dependent. When the phosphor paint is excited with long-wave ultraviolet light, it emits, in this case, a yellow-green light of a given brightness level. As the paint temperature increases, the brightness of the emitted light decreases. Therefore, by measuring the paint brightness, one can obtain thermal contour distributions of a model to which the paint is applied. The contours are then related to model heat flux through the data measured directly by model heat-transfer gage instrumentation (see Fig. 7c). A more detailed explanation of this technique is presented in Ref. 1. On runs using the thermographic phosphor paint, only the top half of the model (above  $\theta = \pm 90$  deg) was sprayed with paint (Fig. 4).

### 3.0 PROCEDURE

#### 3.1 TEST PROCEDURES

The test objectives were to define the surface pressure and heat-transfer-rate distributions on the external tank at angles of attack from 0 to -180 deg with combinations of roll angles from 0 to 90 deg. This was to represent a tumbling reentry trajectory of the tank after separation from the NASA orbiter. The model was tested for angles of attack from 0 to -90 deg in 30-deg increments and then rotated 180 deg in the horizontal plane at the model-sting attachment before proceeding to angles of attack from -90 to -180 deg, in 30-deg increments. The model was tested at various roll angles (0 to 90 deg) at angles of attack from -30 to -150 deg. The combination of angle of attack and

roll determined the model-sting setting required and the model-sting attachment location (see Figs. 3 and 4).

The test was conducted at a nominal Mach number of 16 in the conical nozzle. No source flow corrections were applied to the data. The model was tested at all the desired angles of attack and roll combinations at a free-stream length Reynolds number condition of approximately  $1.10 \times 10^6$ . Five runs were made at a lower length Reynolds number condition of approximately  $0.38 \times 10^6$  to determine Reynolds number effect on the measured parameters. A test summary indicating the test variables is given in Table 3.

### 3.2 TEST CONDITIONS

The method of determining the tunnel flow conditions is briefly summarized as follows: instantaneous values of reservoir pressure ( $p_o$ ) and free-stream pitot pressure ( $p'_o$ ) are measured and an instantaneous value of the stagnation heat transfer rate ( $\dot{q}_o$ ) is inferred from a direct measurement of a shoulder heat rate on a 1.0-in.-diam hemisphere-cylinder heat probe. Total enthalpy ( $H_o$ ) is calculated from  $p'_o$ ,  $\dot{q}_o$ , and the heat probe radius, using Fay-Riddell theory, Ref. 4. The value of  $H_o$  determined in this manner and the measured value of reservoir pressure are then used to determine corresponding values of reservoir temperature, density, and entropy from tabulated thermodynamic data for nitrogen (Ref. 5). The reservoir conditions, the measured value of  $p'_o$ , and the assumption of isentropic flow in the nozzle are then used to compute the free-stream conditions. The basic procedure followed in this computation is given in Refs. 6 and 7. A summary of tunnel conditions is given in Table 4.

### 3.3 DATA ACQUISITION

All test data were recorded on a 70-channel digital system capable of scanning all channels in 1 msec and storing up to 150 scans of data. Basic data reduction was done offline on a digital computer. As a backup to the digital system, as well as to provide a quick look at the data results, the output of each data channel was recorded on an oscillograph. Figure 6 represents examples of the analog traces for the tunnel monitor information ( $p_o$ ,  $p'_o$ , and  $\dot{q}_o$ ) and representative traces of the model surface pressure and heat-transfer gage output histories. Calculated values of free-stream unit Reynolds number ( $Re_\infty/ft$ ) and Mach number ( $M_\infty$ ) are shown to illustrate timewise variations of test conditions. Note that there is a 70-msec delay from the initial pressure rise to the start of the useful run; this delay is caused by the nozzle starting process and the time required for the free-stream temperature to equal or exceed the theoretical saturation temperature of nitrogen.

Thermographic phosphor paint data were recorded in the form of photographic film optical density contours on black-and-white negative film using 80-, 100-, 150-, and 250-mm Hasselblad cameras. The areas of interest were photographed through ports in the top of the test section with four light sources placed as shown in Fig. 4.

The paint data consisted of a "tare" photograph, Fig. 7a, taken prior to the run at room temperature to record the initial paint brightness level. Then at some desirable time in the run another photograph was taken to record the run brightness level. The photographs record paint brightness in terms of film optical density; i.e., the brighter a region is on the model, the denser or darker it will appear on the negative. The system used to reduce the photographic data is a visual display Datacolor System 703-22<sup>®</sup>. The Datacolor System is a closed-circuit television network consisting of a camera and a color monitor console. The cameras read the film optical density across the model surface (i.e., paint brightness). The continuous camera signal is then broken into a preselected number of color steps (32 maximum), and the results are displayed on the monitor. The monitor is then photographed to record the model heating distribution, (Fig. 7b).

### 3.4 DATA PRECISION

Laboratory calibrations using static loads indicate an uncertainty of  $\pm 1$  percent for the pressure transducers. Similarly, the laboratory uncertainties in the heat-transfer-rate gages are  $\pm 5$  percent. The uncertainties in the tunnel measured data, however, are higher because of the dynamics of the measurements and system errors. The uncertainties in the monitor probe measurements ( $p'_o$  and  $\dot{q}_o$ ) and arc-chamber measurements ( $p_o$ ) were estimated considering both the static load calibrations and the repeatability of the test section pitot profiles. The uncertainties in the pressure data ( $p'_o$  and  $p_o$ ) are estimated to be  $\pm 4$  and  $\pm 5$  percent, respectively, based on an average of two measurements; the heat-transfer rate ( $\dot{q}_o$ ) is  $\pm 5$  percent based on an average of four measurements. These values were used to estimate uncertainties in the tunnel flow parameters using the Taylor series method of error propagation. Representative parameters are given below in percent uncertainty.

$T_o$	$p_o$	$p'_o$	$\dot{q}_o$	$p_\infty$	$q_\infty$	$V_\infty$	$M_\infty$	$Re_{\infty, \ell}$
$\pm 4$	$\pm 5$	$\pm 4$	$\pm 5$	$\pm 6$	$\pm 4$	$\pm 3$	$\pm 1.5$	$\pm 10$

The model attitude position was set prior to each run; the pitch, yaw, and roll angles are estimated to be accurate within  $\pm 0.10$  deg.

Tables 2c and d include the percent uncertainty values for the various ranges of surface heat-transfer rate and pressure measurements. The uncertainty values depended

on the absolute levels measured during the run relative to the design range of the particular type of gage. In addition, the heat gage uncertainties were dependent on the use of preamplifiers. Uncertainty levels are also shown for the ratios  $\dot{q}/\dot{q}_0$  and  $p/p'_0$ , which were determined by combining the indicated uncertainties in the tunnel flow parameters with the model heat-transfer rates and pressures, respectively, by the Taylor series method of error propagation.

In general, the thermographic paint data can be no more accurate than the heat-transfer-rate data used to establish the paint calibrations. The color band widths from the Datacolor system do introduce some uncertainty into the paint data. The uncertainty in the final paint data depends upon the number of colors used, determining in which color the calibrating gages are located, the uncertainty of the calibration gages, the number of calibrating gages, and the ability to determine the midpoint of a color band width. Obviously, some of the above contributing factors to paint uncertainty are interrelated. Based on previous experience, the uncertainty in the paint data is on the order of  $\pm 15$  to  $\pm 20$  percent, but the uncertainty, presently, is best estimated graphically for each run from the paint calibration (for example, see Fig. 7c).

#### 4.0 RESULTS AND DISCUSSION

The NASA external tank pressure and heat-transfer-rate data are shown in Figs. 7 through 13 for several combinations of angle of attack and roll. The surface pressure measurements are shown normalized by the measured pressure behind a normal shock in the test section ( $p'_0$ ). The surface heat-transfer rates are normalized by the measured stagnation heat-transfer rate on a 1.00-in.-diam hemisphere-cylinder test section probe ( $\dot{q}_0$ ). All results presented herein were obtained at  $M_\infty \approx 16$  and  $Re_{\infty, \ell} \approx 1.1 \times 10^6$ . Four runs were made at a reduced Reynolds number ( $Re_{\infty, \ell} \approx 0.38 \times 10^6$ ) and exhibited no discernible difference in normalized pressure and heat-transfer-rate levels when compared with the higher Reynolds number results.

Figure 7 shows the interference heating regions around the forward protuberances obtained by the phosphor paint technique at  $\alpha' = -30$  deg and  $\phi' = 0$ . Figure 7a shows the region of analysis, which includes the forward tiedown, fuel line, and wire tunnel. Heat transfer contours are defined in Fig. 7b by means of the Datacolor System. Heat-transfer gages appear as dark blue spots on the photograph. The output of these gages is plotted versus color in Fig. 7c to obtain the calibration curve, which is seen to be linear over the range of data. The  $\pm 15$ -percent scatter in the data is typical. Note that the "hot spot" indicated by yellow is in a region not monitored with heat-transfer instrumentation and that definition of the heat-transfer level in this region requires an extrapolation through three color bands. The maximum heating rate as defined by the

paint analysis of Fig. 7c at  $\alpha' = -30$  deg is shown in Fig. 8a. Since there were no heat-transfer gages initially located in this region, the hot spot does not appear in the analysis of gage results. As a result of the very high heating rate observed from the paint analysis, two additional heat-transfer-rate gages were added in the hot region to measure the high heat-transfer rates on subsequent runs. The additional instrumentation corroborated the high heat-transfer rates from the phosphor paint results at other model attitudes as documented in Figs. 8 and 9. This clearly demonstrates the value of the phosphor paint results in defining areas of interference heating. Other high heat-transfer-rate regions at different model attitudes in uninstrumented areas were similarly defined using the phosphor paint technique.

Windward centerline heat-transfer and pressure distribution data are shown in Fig. 8 for angles of attack from 0 to  $-180$  deg, with zero roll. The increase in the surface heat-transfer rate immediately downstream of the forward orbiter tiedown is quite dramatic at the lower angles of attack. An order of magnitude increase over the local values is indicated at  $\alpha' = 0$  while at  $\alpha' = -30$  deg a factor of four is noted. The rear support structure was also a cause of increased local surface pressures and heating rates. For  $\alpha' = 0$  and  $-30$  deg the heating rate adjacent to the rear support and cross member was approximately a factor of 5 or more greater than the local values. The effect of the protuberances on the local pressure and heat-transfer measurements decreased as angle of attack approached  $-90$  deg, then increased again with greater angles with the forward tiedown being the main source of interference. As is shown in Figs. 7 and 8, the high heating rate caused by the forward tiedown was very localized. There were no pressure orifices in the immediate area to record the surface pressure due to this interference. The interference of the orbiter tiedown structures on the windward centerline measurements are clearly indicated in Fig. 8 for angles of attack of zero and  $-180$  deg by comparing the data for the external tank model with data for the clean model (all external protuberances removed).

Data were obtained at various total angles of attack,  $\alpha'$ , for various aerodynamic roll angles,  $\phi'$ . The model centerline ( $\theta = 0$ ) pressure and heat-transfer distributions are given in Fig. 9 for angles of attack of  $-30$ ,  $-90$ , and  $-150$  deg and four roll angles. The interference caused by the forward and aft tiedown structures is substantial even at a roll angle of  $90$  deg for  $\alpha' = -30$  and  $-150$  deg. The aft support is the main contributing factor to the interference observed at  $\alpha' = -90$ . Comparison is made at each angle of attack for the  $90$ -deg roll case with runs made with a clean model (all external protuberances removed).

The measured heat-transfer rates and pressure data at approximate  $x/\ell$  stations of 0.10 and 0.35 are plotted against the model circumferential angle  $\theta$  in Fig. 10 for  $\alpha'$

= 0. Comparison is shown with a run made with a clean model, indicating negligible effect of the external protuberances at these respective axial stations.

The external tank peripheral heat-transfer and pressure distributions for  $\alpha' = -30$  deg are presented in Fig. 11 for approximate  $x/\ell$  stations of 0.10 and 0.35. The  $x/\ell$  station of 0.10 is on the ogive nose, whereas  $x/\ell = 0.35$  is on the circular cylinder region of the model, upstream of the forward support structure. The data are plotted versus angular distance from the stagnation line  $\theta^*$ , which is equal to the circumferential angle  $\theta$  plus the aerodynamic roll angle  $\phi'$ . This enables all roll angle run data at a given angle of attack to be represented on one plot. At an angle of attack of -30 deg on the ogive nose section ( $x/\ell \approx 0.10$ ) the pressure and heat-transfer distributions reached a peak at the stagnation line ( $\theta^* = 0$ ) and decreased continuously from that value. Little deviation is noted when the protuberance model distribution is compared to the clean model distribution, which indicates only minor local effects caused by the fuel lines crossing this station. The heat-transfer distribution is very systematic even throughout the separated flow region. It should be noted that in the presentation of the data versus  $\theta^*$  the physical locations of the structures, etc., are at different  $\theta^*$  values for each combination of angle of attack and roll.

Data are presented in Fig. 11b for  $\alpha' = -30$  deg for the  $x/\ell$  station of 0.35 (circular cylinder). The pressure distribution is compared with a correlation of experimental circular cylinder data for various normal Mach numbers and yaw angles presented by Beckwith and Cohen (Ref. 8) which included yaw angles from zero to 60 deg ( $\alpha' = -90$  to -30 deg) and a range of normal Mach numbers from 3.5 to 6.9. The Modified Newtonian theory pressure distribution  $[p/p_s = (1 - p_\infty/p_s) \cos^2 \theta^* + p_\infty/p_s]$  is also shown for comparison. The stagnation line value ( $p_s$ ) was determined from the normal Mach number and perfect gas relationship (Ref. 9). The heat-transfer-rate distribution decreased continuously from the stagnation line to the separated flow region, where the distribution becomes much more erratic. Larger uncertainties are also associated with the measurements at the lower levels in this region.

Data are shown on similar plots for  $\alpha' = -60$  deg in Fig. 12. A small perturbation in the heat-transfer-rate level at  $\theta^* = 45$  deg is indicated for the data at  $x/\ell = 0.10$  and  $\phi' = 0$  in Fig. 12a. Also, a peak is noted at  $\theta^* = 180$  deg in the separated region. Presented in Fig. 12b are similar plots for  $x/\ell = 0.35$  where the pressure distribution is compared to Beckwith's correlation of cylinder distributions (Ref. 8) and the modified Newtonian expression.

Circumferential heat-transfer and pressure distribution data are shown in Fig. 13 for  $\alpha' = -90$  deg at three  $x/\ell$  stations. As was shown for  $\alpha' = -30$  and -60 deg, the heat-transfer



distributions for  $\alpha' = -90$  deg are essentially symmetrical about  $\pm 90$  deg from the stagnation line on the ogive nose ( $x/\ell \approx 0.10$ ) with small perturbations caused by the local structures. The heat-transfer and pressure distributions at all stations are well defined to approximately 120 deg from the stagnation line before becoming somewhat erratic in the separated region.

The measured heat-transfer distributions at  $x/\ell = 0.35$  and  $0.75$  at  $\alpha' = -90$  deg are shown in Fig. 13b and c, respectively, and are compared with the theories of Beckwith (Ref. 8) and Lees (Ref. 10). Lees' distribution theory provides better agreement with the measured distribution to about  $\theta^* \approx 120$  deg. The two-dimensional stagnation heat-transfer rate ( $\dot{q}_s$ , used to nondimensionalize the Beckwith and Lees theories) was determined using the implicit finite difference integration of the infinite yawed body laminar boundary-layer equations following Adams (Ref. 11).\*

Pressure distributions are also included in Fig. 13b and c for  $x/\ell = 0.35$  and  $0.75$  at  $\alpha' = -90$  deg and are compared with Beckwith's correlation and the modified Newtonian expression. Comparison is also made to Hamaker's theory for flow of a perfect gas over a circular cylinder at infinite Mach number (Ref. 12). The pressure distribution from Refs. 8 and 12 compared well with that measured, not only for  $\alpha' = -90$  deg but also for  $\alpha' = -30$  and  $-60$  deg in the circular cylinder section. For all angles of attack the modified Newtonian expression substantially underestimates the pressure for  $\theta^*$  greater than 45 deg.

The circumferential heat-transfer-rate and pressure data previously shown in Figs. 11b, 12b, and 13b for the circular cylinder section of the model ( $x/\ell = 0.35$ ) are shown in Fig. 14 normalized to the measured stagnation line values for the respective runs for  $\theta^* = 0$  to 120 deg. Comparison is again made with Beckwith's correlation for a clean circular cylinder pressure distribution and Lees' laminar heat-transfer theory. Beckwith's pressure distribution generally agrees with the present pressure distributions indicating little or no dependence on angle of attack. The clean body heat-transfer-rate data indicate that the circumferential heat-transfer distribution is also essentially independent of angle of attack. The heat-transfer-rate data for the model with external structures generally lies below the smooth data within a reasonable scatter band.

## 5.0 CONCLUSIONS

Local heat transfer and static wall pressures have been measured on a model of the NASA Shuttle external tank at angles of attack of 0, -30, -60, -90, -120, -150, and -180 deg with various combinations of roll angles from 0 to 90 deg. The tests were made at a free-stream Mach number of 16 and Reynolds numbers of  $0.38 \times 10^6$  to  $1.1 \times 10^6$  based on model length.

---

\*Dr. John Adams of AEDC-VKF supplied these calculations.

The windward centerline heat-transfer and pressure distributions were strongly influenced by the various attachment structures at certain combinations of angle of attack and roll. Heat-transfer-rate increases of an order of magnitude over clean body values were observed at areas near the two orbiter tiedown structures.

The circumferential pressure and heat-transfer-rate distributions on the circular cylinder section of the model,  $x/l = 0.35$ , were essentially independent of angle of attack in terms of the angular distance  $\theta^*$ , both for the clean model and for the model with external protuberances. Previous experimental pressure and theoretical laminar heat-transfer distributions on a clean body agreed well with measured clean model values. The stagnation line rates were always the maximum value measured with the chordwise distribution decreasing continuously from this angular location to some separation line.

Use of the phosphor paint technique made it possible to define hot regions in uninstrumented regions of the model. Placing additional instrumentation in the hot region underneath the forward tiedown provided better definition of the maximum heat-transfer rate in this region.

#### REFERENCES

1. Pate, S. R. and Eaves, R. H., Jr. "Recent Advances in the Performance and Testing Capabilities of the AEDC-VKF Tunnel F (HOTSHOT) Hypersonic Facility." AIAA Paper No. 74-84, presented at the AIAA 12th Aerospace Sciences Meeting, Washington, D.C., January 30 - February 1, 1974.
2. Ledford, R. L., Smotherman, W. E., and Kidd, C. T. "Recent Developments in Heat-Transfer-Rate, Pressure, and Force Measurements for Hotshot Tunnels." AEDC-TR-66-228 (AD645764), January 1967.
3. Bynum, D. S. "Instrumentation for the AEDC/VKF 100-in. Hotshot (Tunnel F)." AEDC-TR-66-209 (AD804567), January 1967.
4. Fay, J. A. and Riddell, F. R. "Theory of Stagnation Point Heat Transfer in Dissociated Air." Journal of the Aeronautical Sciences, Vol. 25, No. 2, February 1958, pp. 73-85, 121.
5. Brahinsky, Herbert S. and Neel, Charles A. "Tables of Equilibrium Thermodynamic Properties of Nitrogen." Vol. I-IV, AEDC-TR-69-126 (AD693134, AD692712, AD692713, AD692172), August 1969.
6. Grabau, Martin, Smithson, H. K., Jr., and Little, W. J. "A Data Reduction Program for Hotshot Tunnels Based on the Fay-Riddell Heat-Transfer Rate Using Nitrogen at Stagnation Temperatures from 1500 to 5000°K." AEDC-TR-64-50 (AD601070), June 1964.

7. Griffith, B. J. and Lewis, Clark H. "Laminar Heat Transfer to Spherically Blunted Cones at Hypersonic Conditions." AIAA Journal, Vol. 2, No. 3, March 1964, pp. 438-444.
8. Beckwith, Ivan E. and Cohen, Nathaniel B. "Application of Similiar Solutions to Calculation of Laminar Heat Transfer on Bodies with Yaw and Large Pressure Gradient in High-Speed Flow." NASA TN D-625, January 1961.
9. Ames Research Staff. "Equations, Tables, and Charts for Compressible Flow." NACA Rep. 1135, 1953.
10. Lees, Lester. "Laminar Heat Transfer Over Blunt-Nosed Bodies at Hypersonic Flight Speeds." Jet Propulsion, Vol. 26, No. 4, April 1956, pp. 259-269, 274.
11. Adams, John C., Jr. and Martindale, William R. "Hypersonic Lifting Body Windward Surface Flow-Field Analysis for High Angles of Incidence." AEDC-TR-73-2 (AD756499), February 1973.
12. Hamaker, Frank M. "Numerical Solution of the Flow of a Perfect Gas Over a Circular Cylinder at Infinite Mach Number." NASA MEMO 2-25-59A, March 1959.

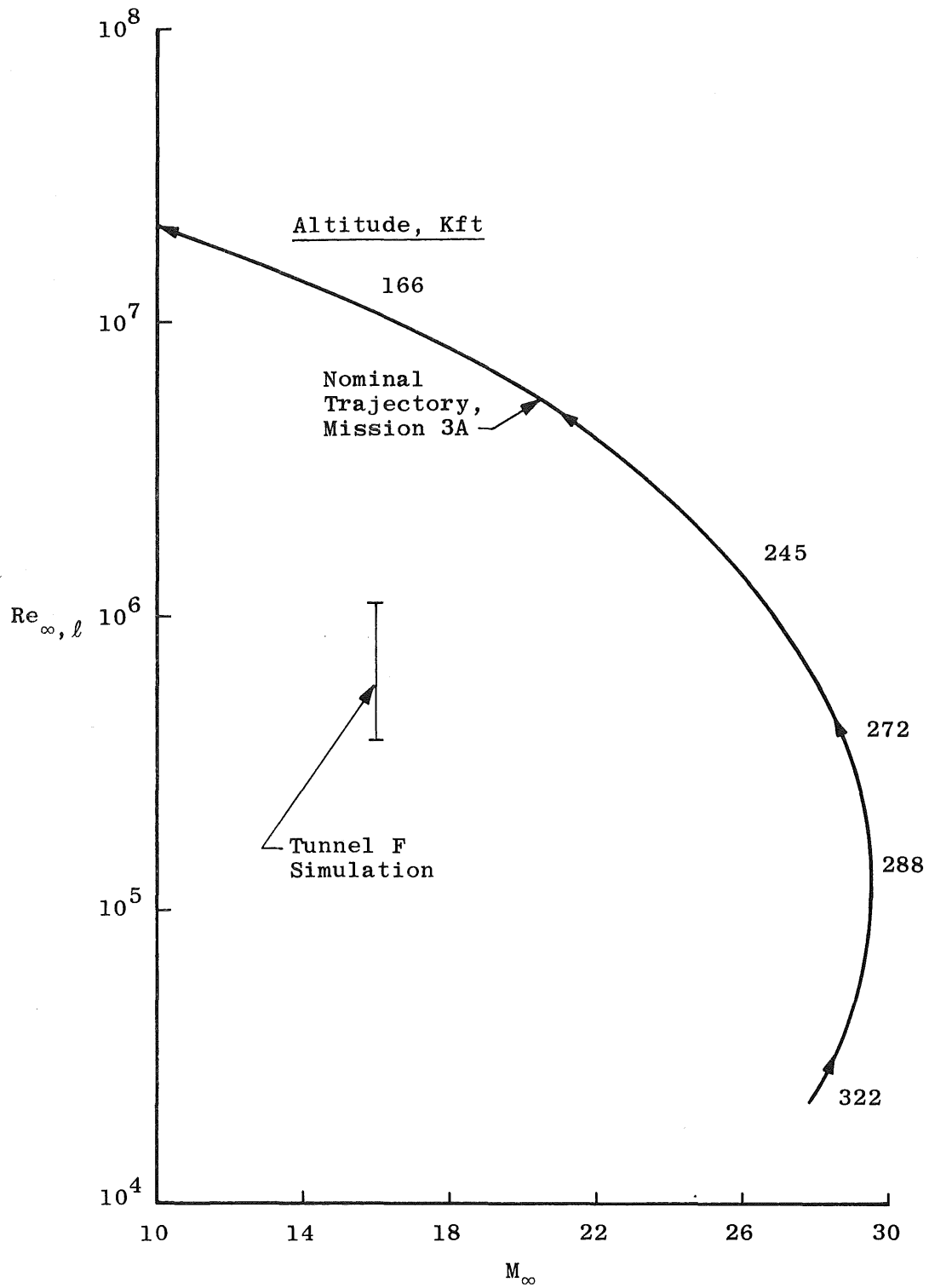


Figure 1. Typical external tank entry trajectory compared with Tunnel F test condition.



Figure 2. Photograph of the NASA external tank 0.015-scale model.

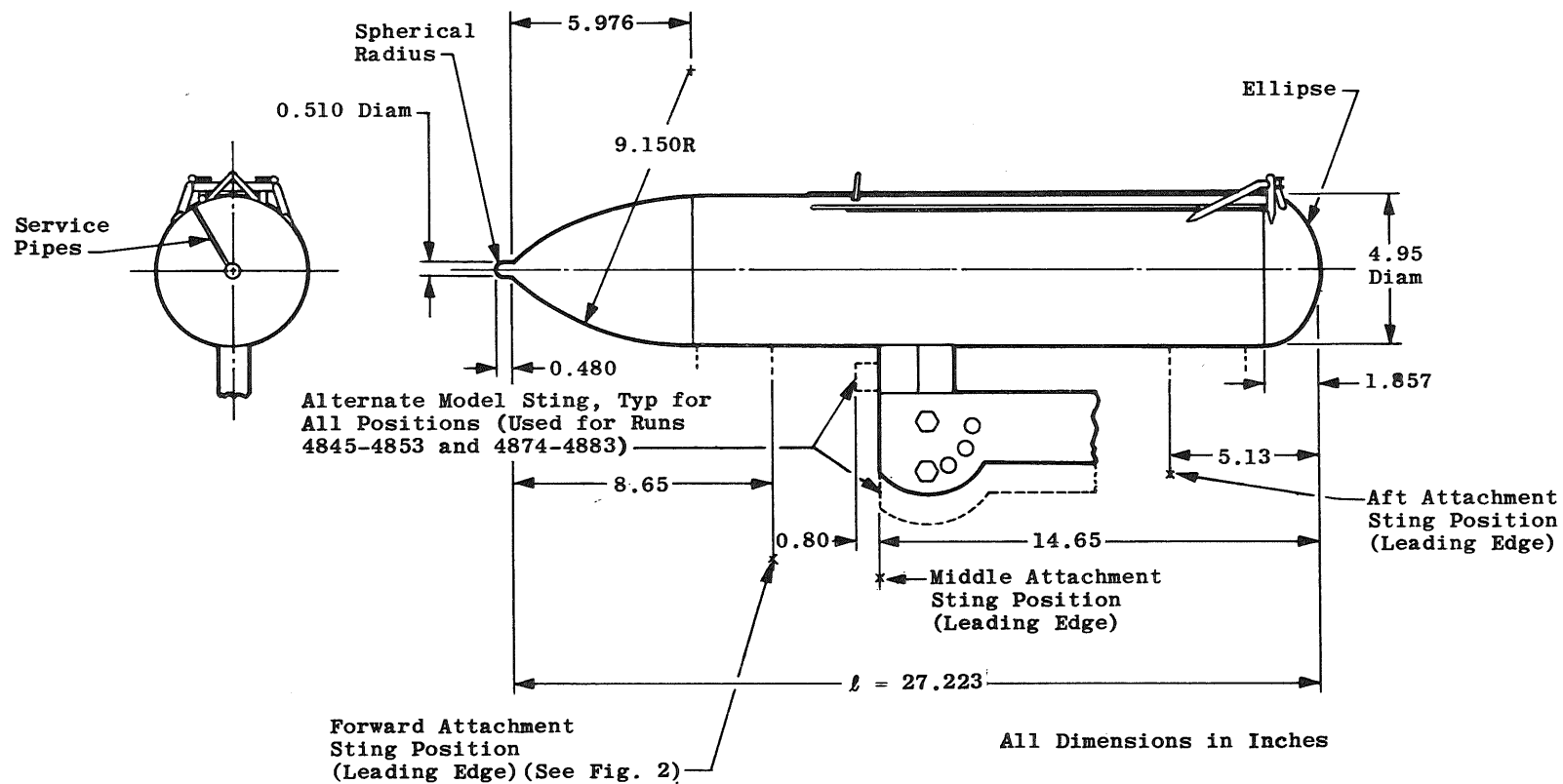


Figure 3. Sketch illustrating model and sting details.

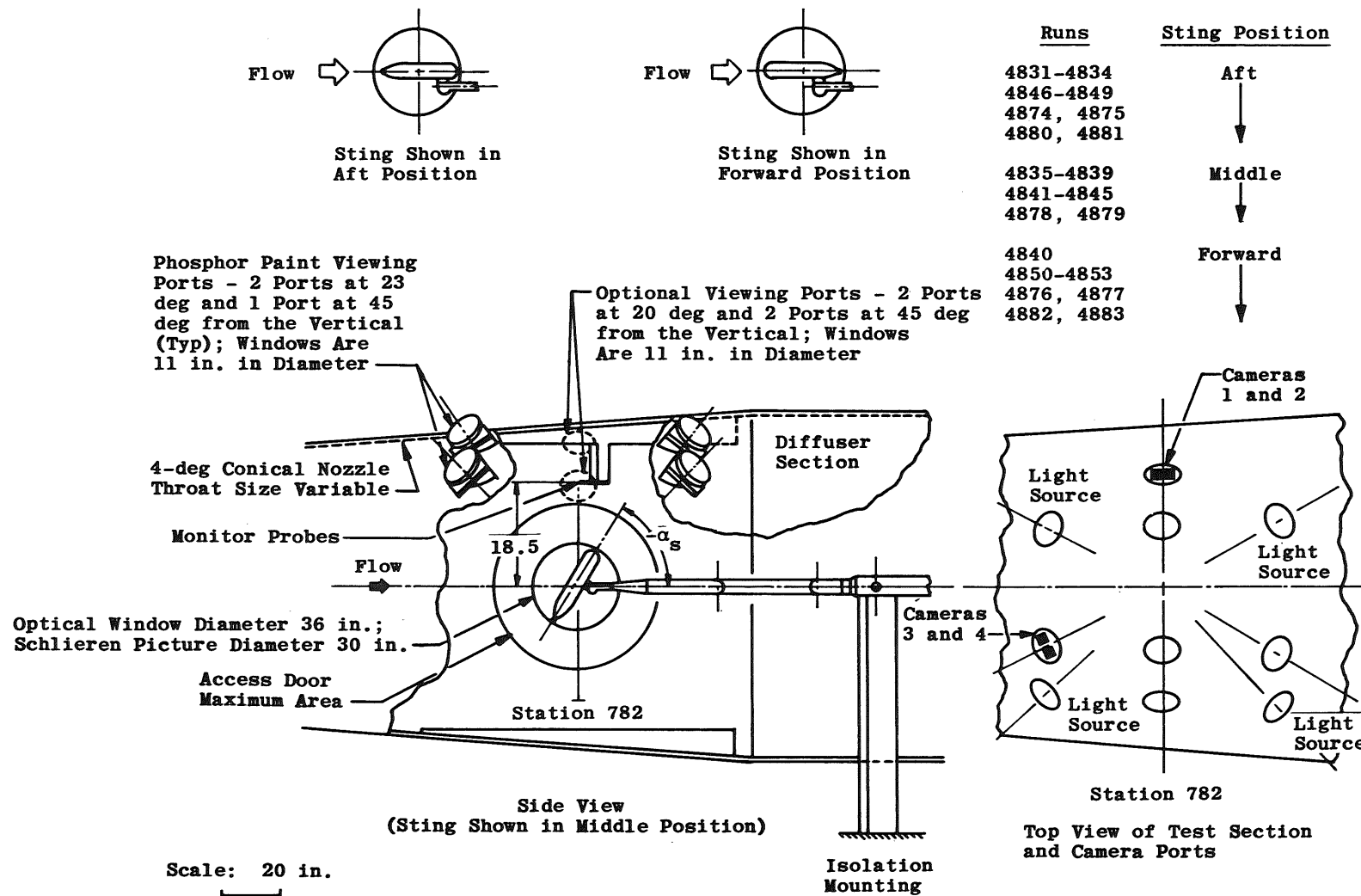


Figure 4. NASA external tank (0.015-scale model) installation in Tunnel F.

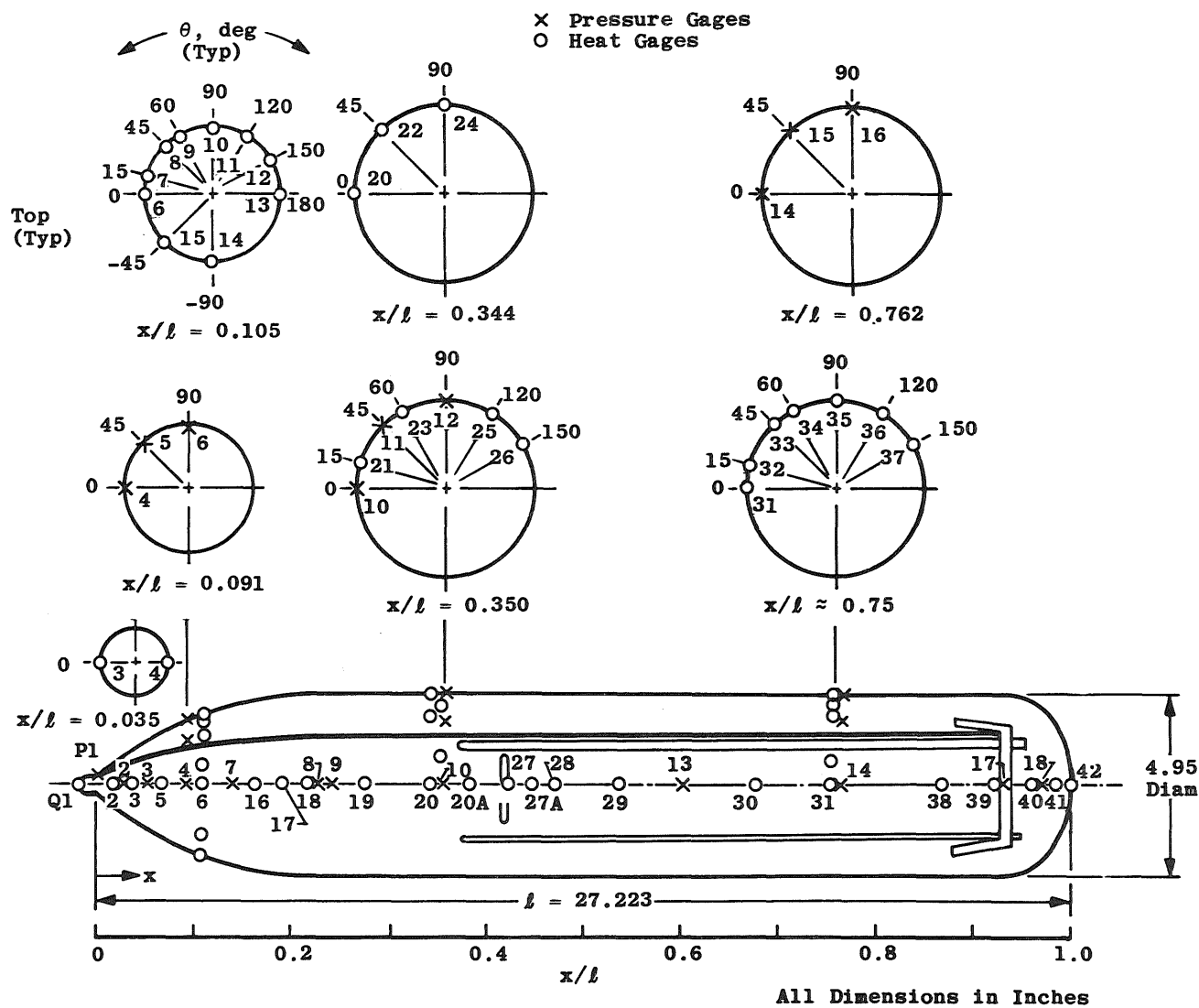


Figure 5. Sketch illustrating pressure and heat-transfer gage locations.



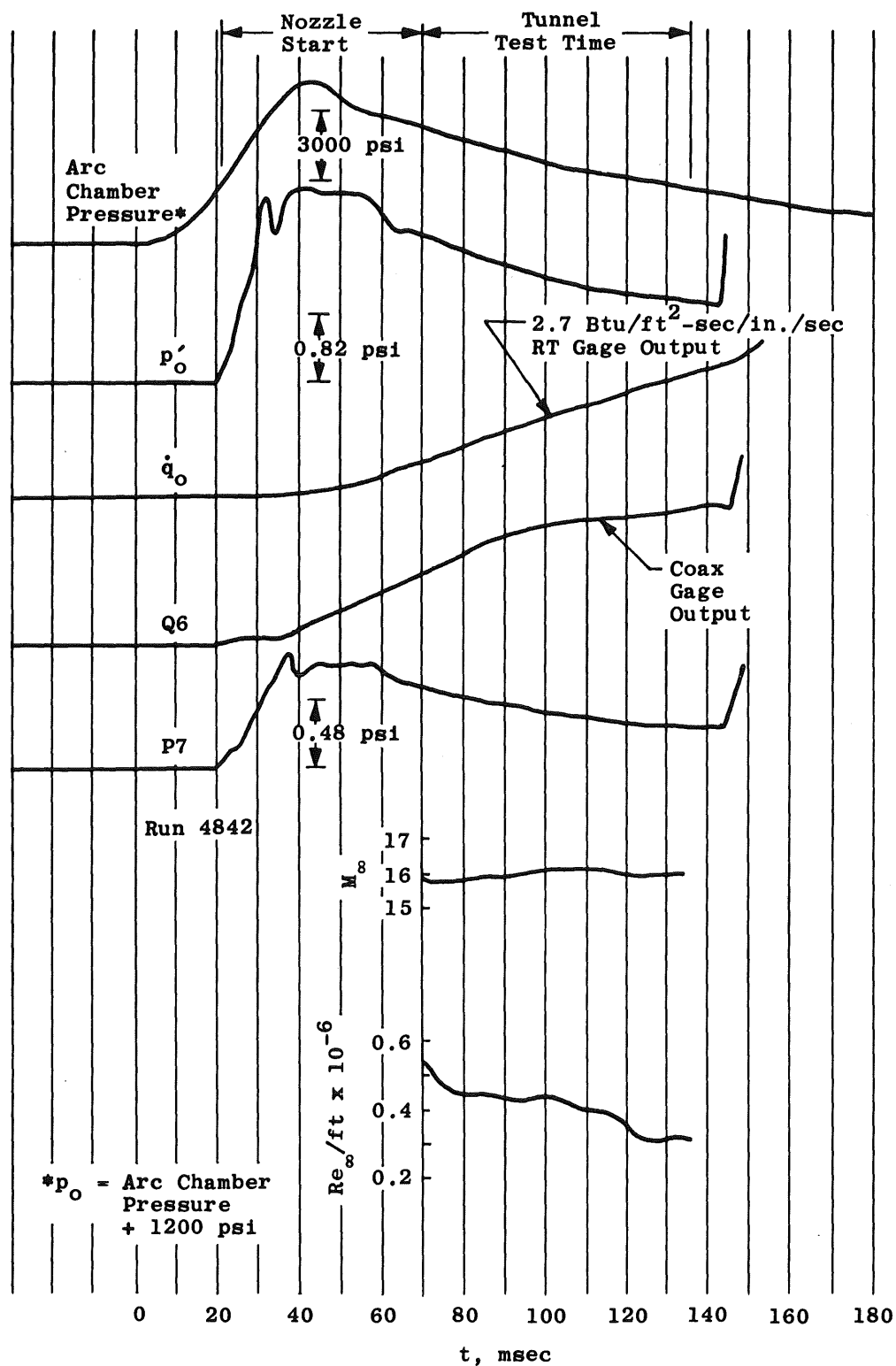
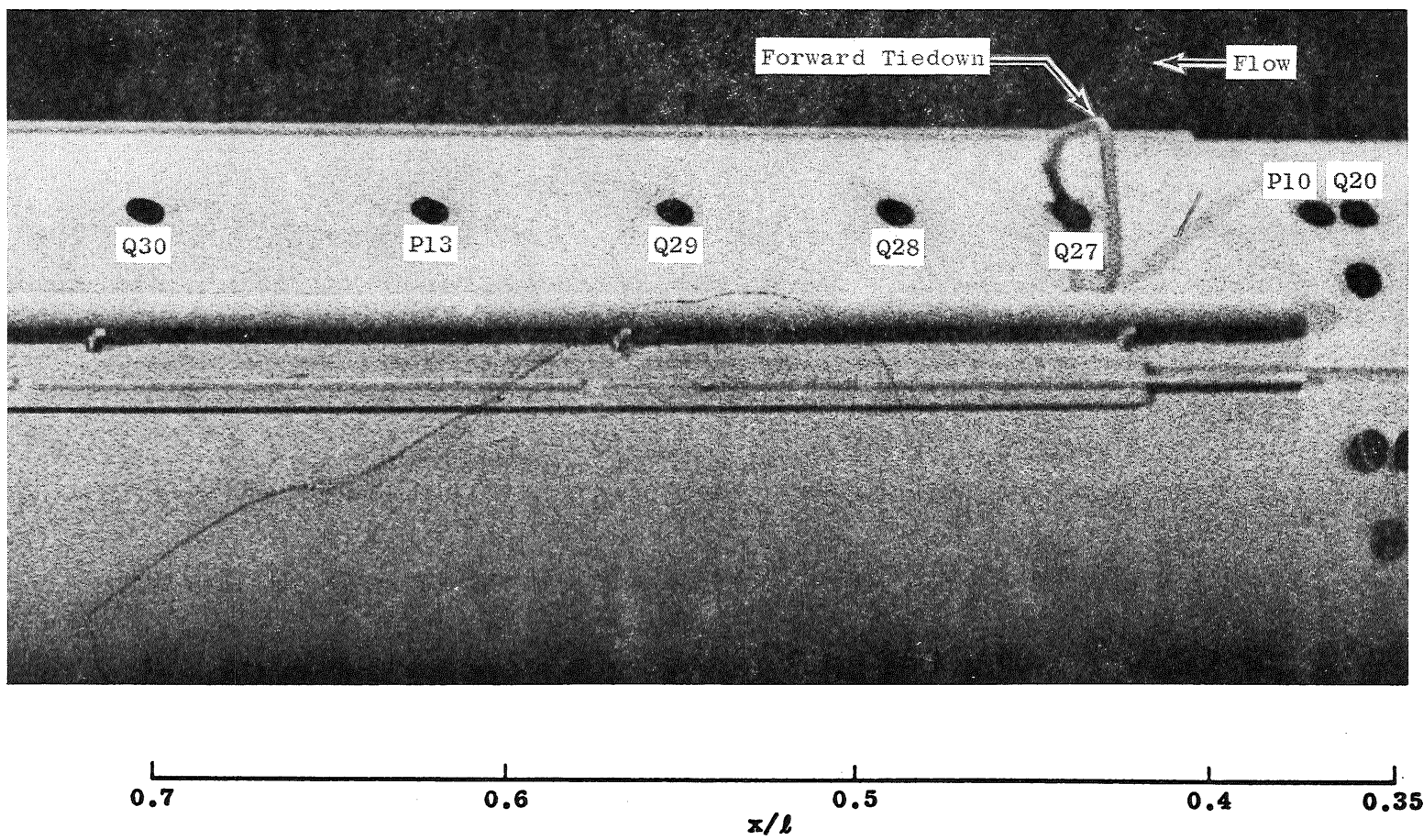
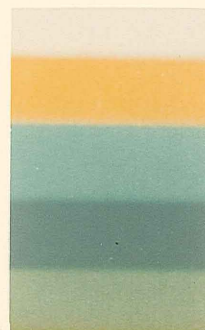


Figure 6. Typical analog data traces and variation of test conditions.

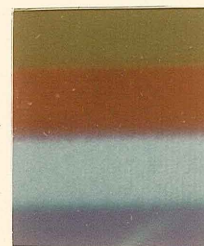


a. Tare photograph

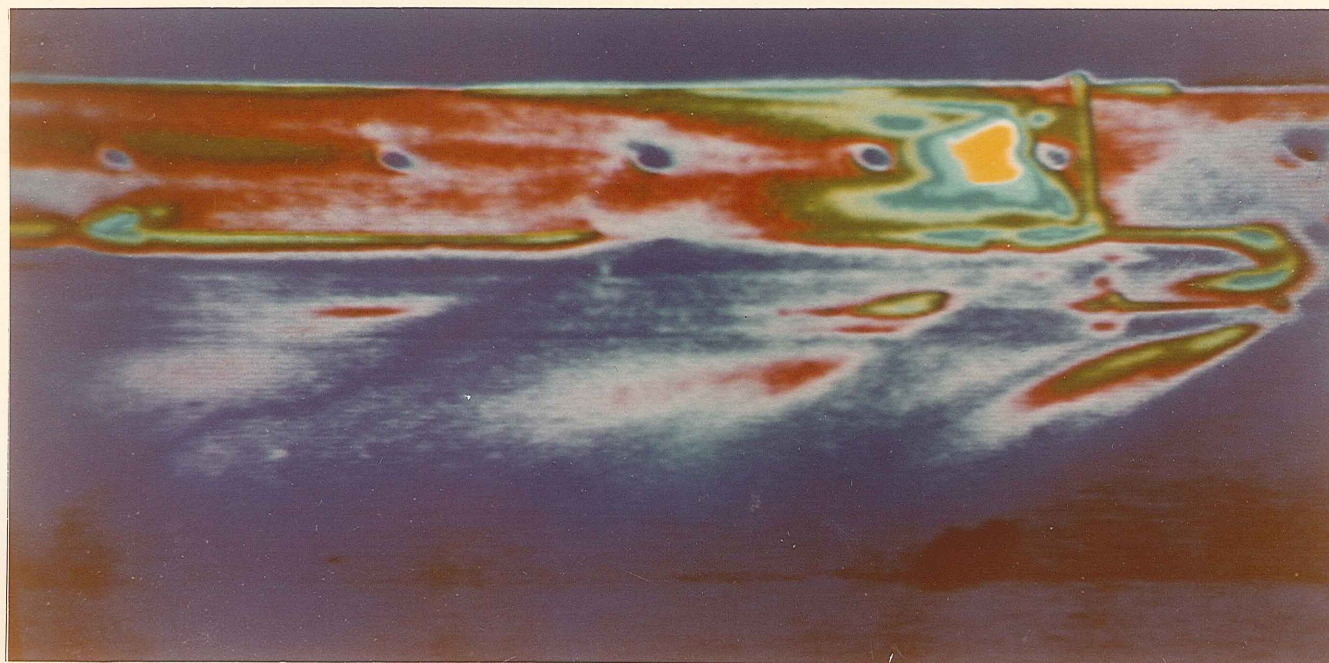
Figure 7. Typical phosphor paint results,  $\alpha' = -30$  deg,  $\phi' = 0$ .



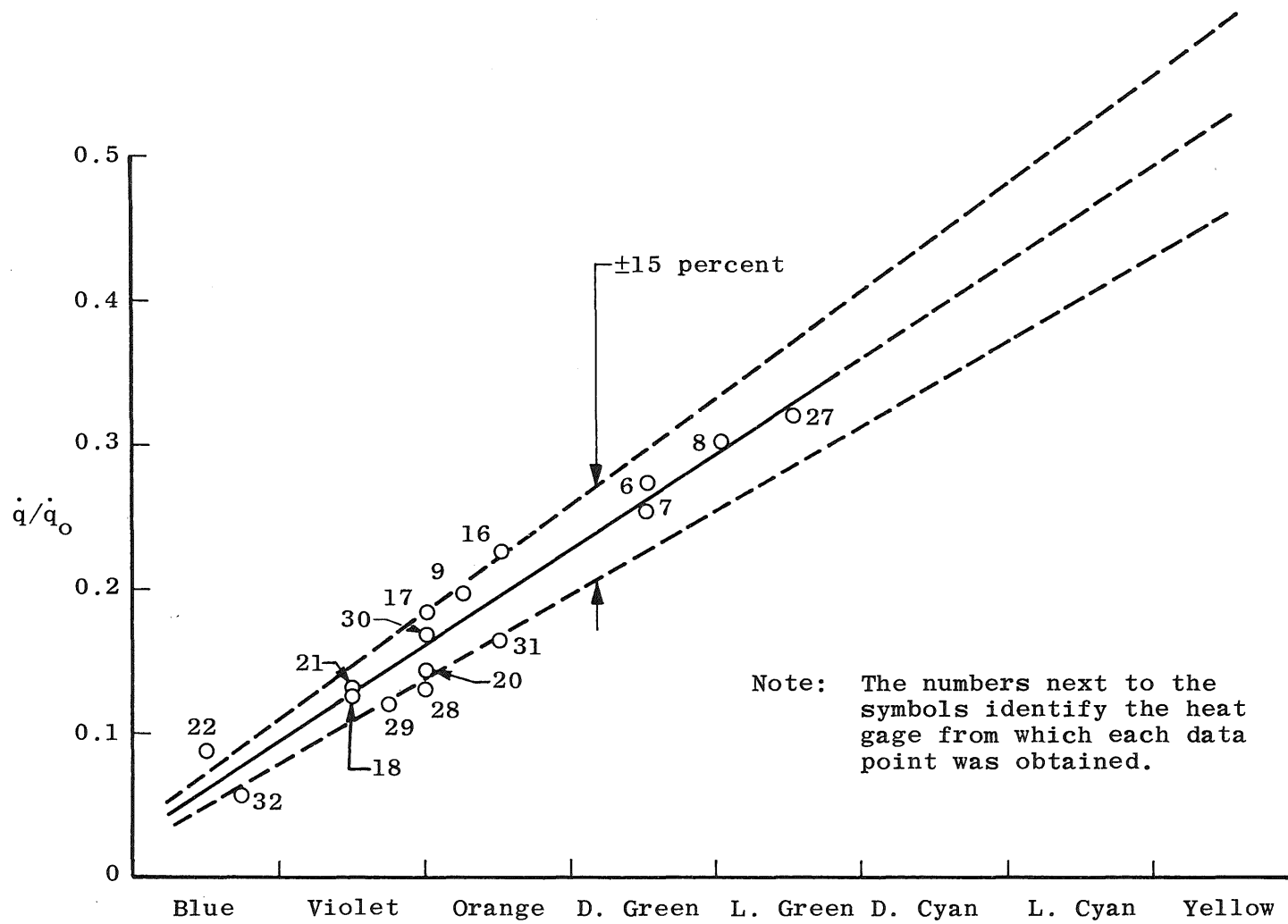
White  
Yellow  
Light Cyan  
Dark Cyan  
Light Green



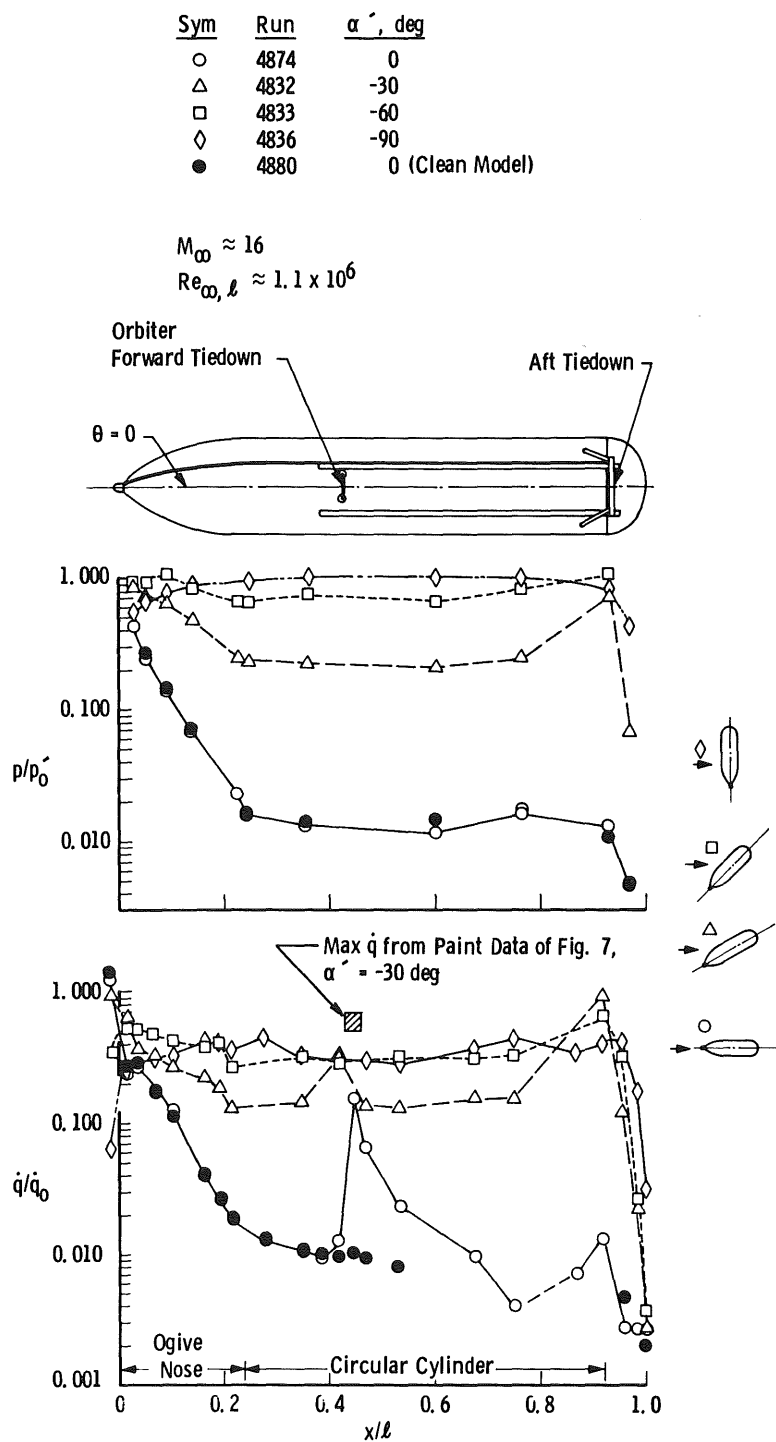
Dark Green  
Orange  
Violet  
Blue



b. Heat-transfer contours  
Figure 7. Continued.



c. Calibration plot  
Figure 7. Concluded.



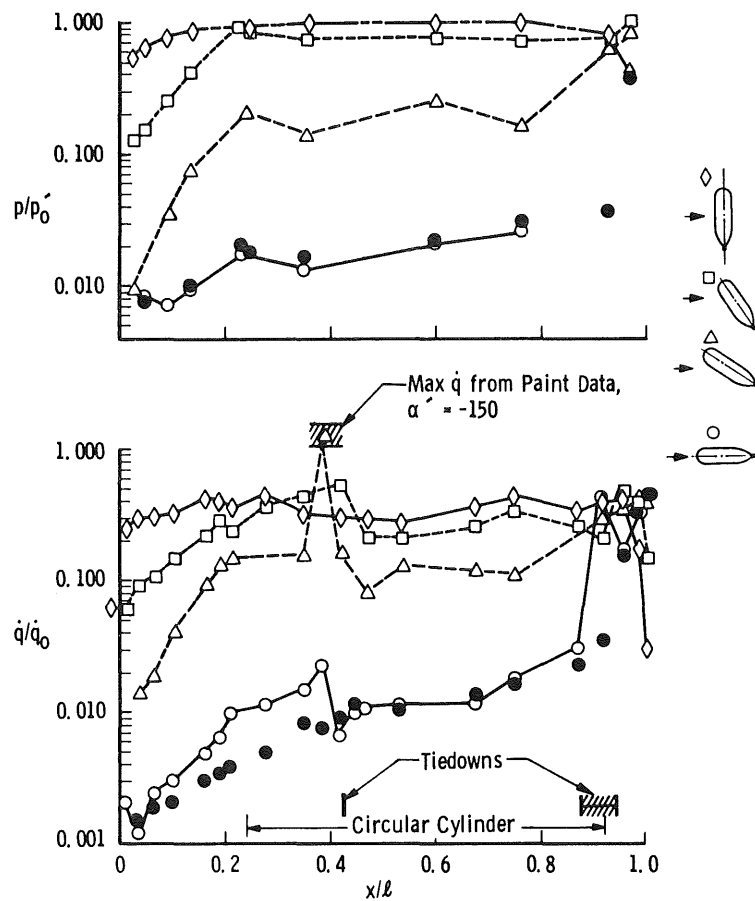
a.  $\alpha' = 0, -30, -60$ , and  $-90$  deg

Figure 8. External tank windward centerline ( $\theta = 0$ ) heat-transfer and pressure distributions.

Sym	Run	$\alpha'$ , deg
◇	4836	-90
□	4838	-120
△	4840	-150
○	4876	-180
●	4882	-180 (Clean Model)

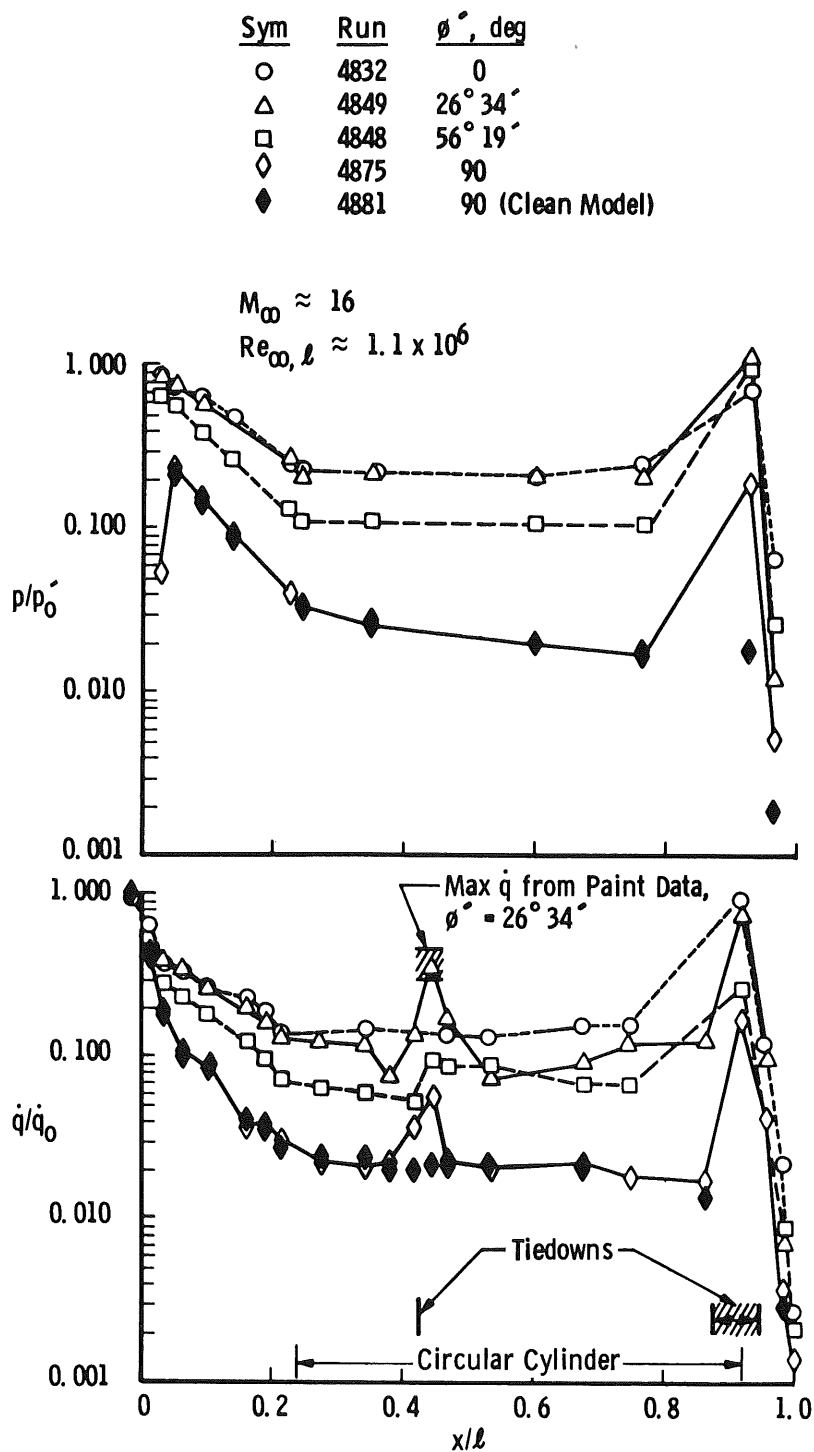
$$M_\infty \approx 16$$

$$Re_{\infty, l} \approx 1.1 \times 10^6$$



b.  $\alpha' = -90, -120, -150, \text{ and } -180 \text{ deg}$

Figure 8. Concluded.

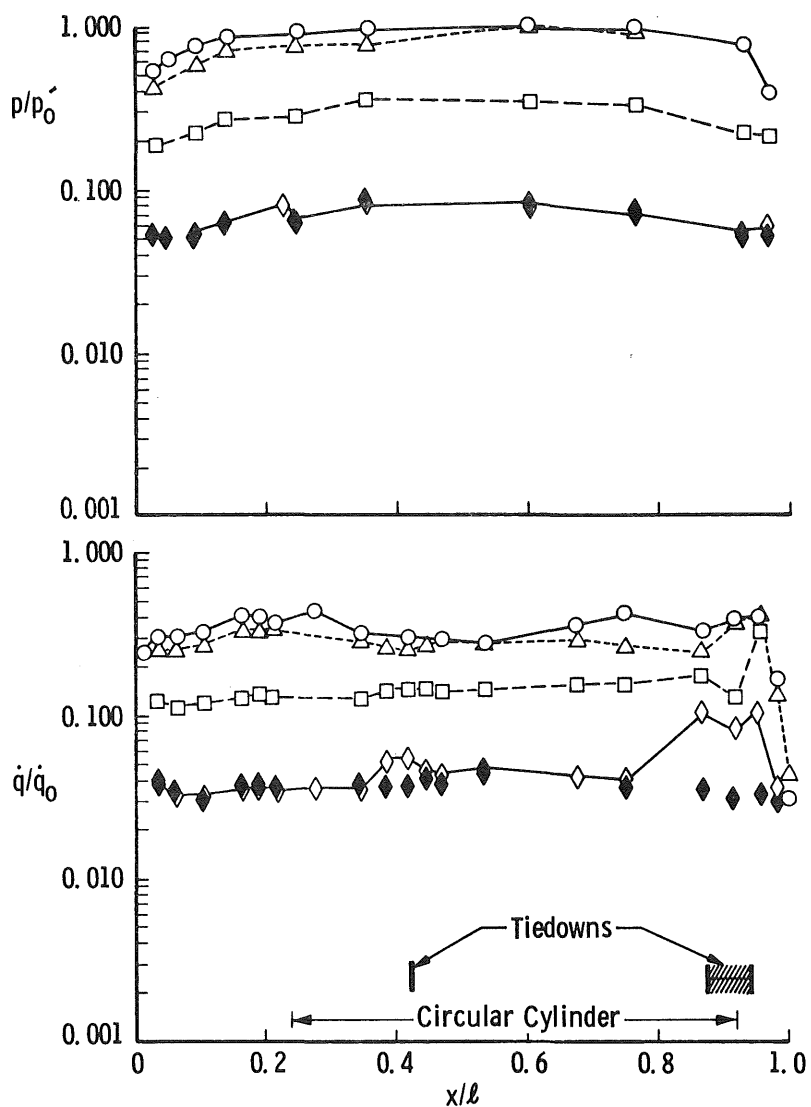


a.  $\alpha' = -30^\circ$

Figure 9. Variation of external tank heat-transfer and pressure distributions on model centerline ( $\theta = 0$ ) with roll angle.

Sym	Run	$\phi'$ , deg
○	4836	0
△	4841	30
□	4842	60
◇	4843	90
◆	4844	90 (Clean Model)

$M_\infty \approx 16$   
 $Re_{\infty, l} \approx 1.1 \times 10^6$

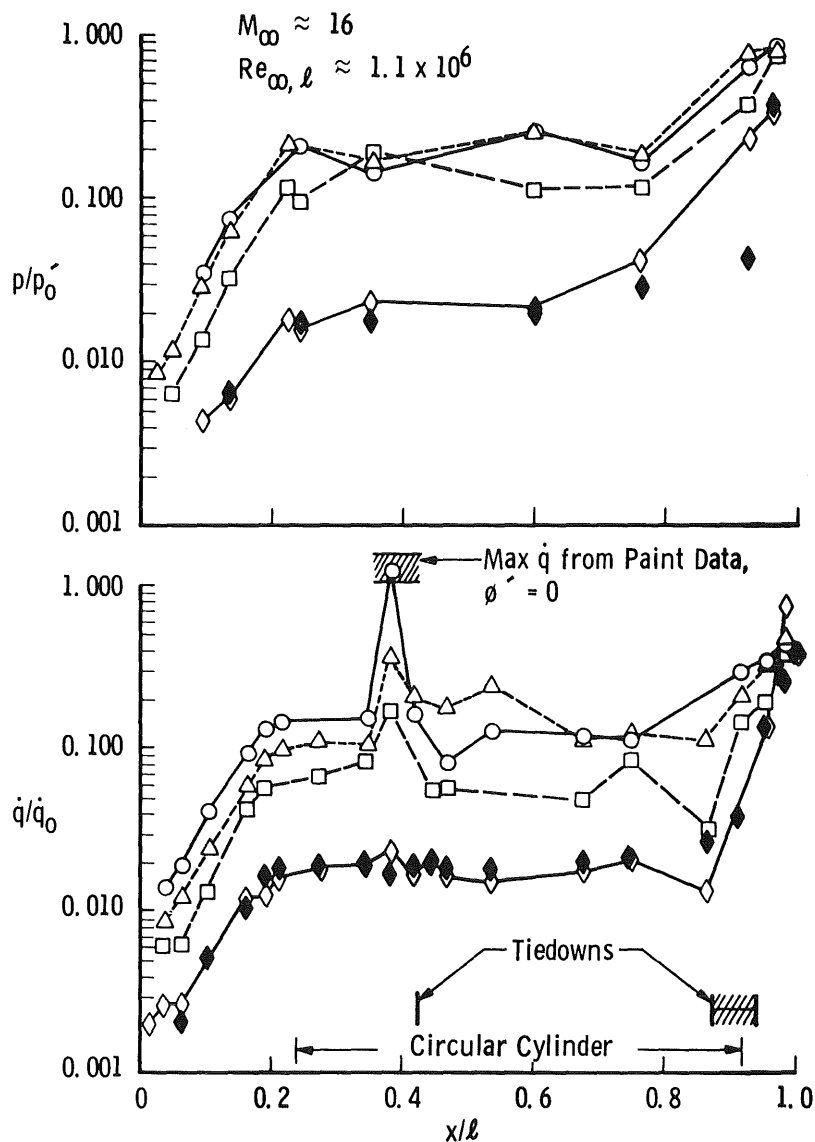


b.  $\alpha' = -90$  deg

Figure 9. Continued.



Sym	Run	$\phi^\circ$ , deg
○	4840	0
△	4851	26° 34'
□	4850	56° 19'
◇	4877	90
◆	4883	90 (Clean Model)



c.  $\alpha' = -150$  deg  
 Figure 9. Concluded.

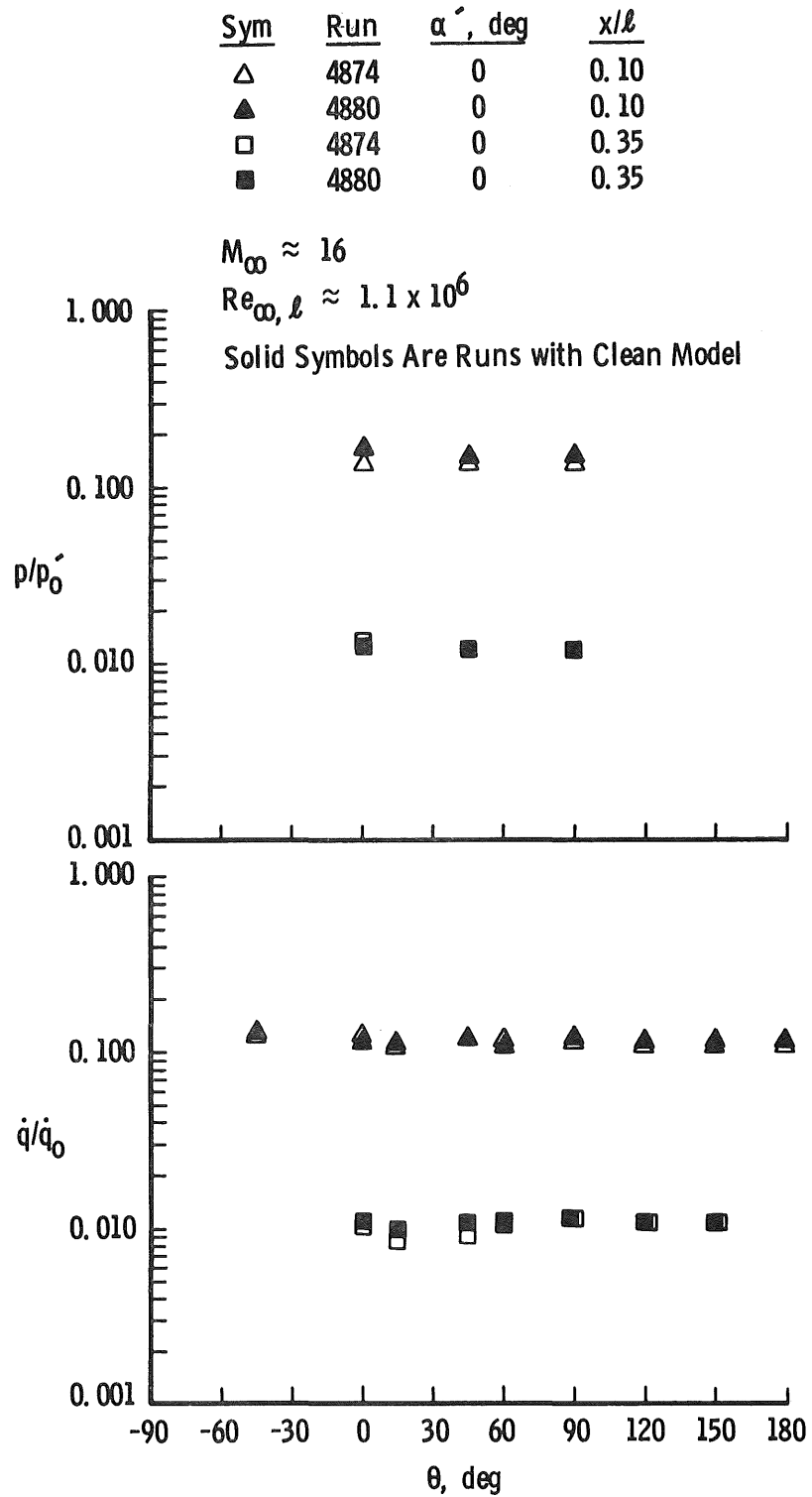
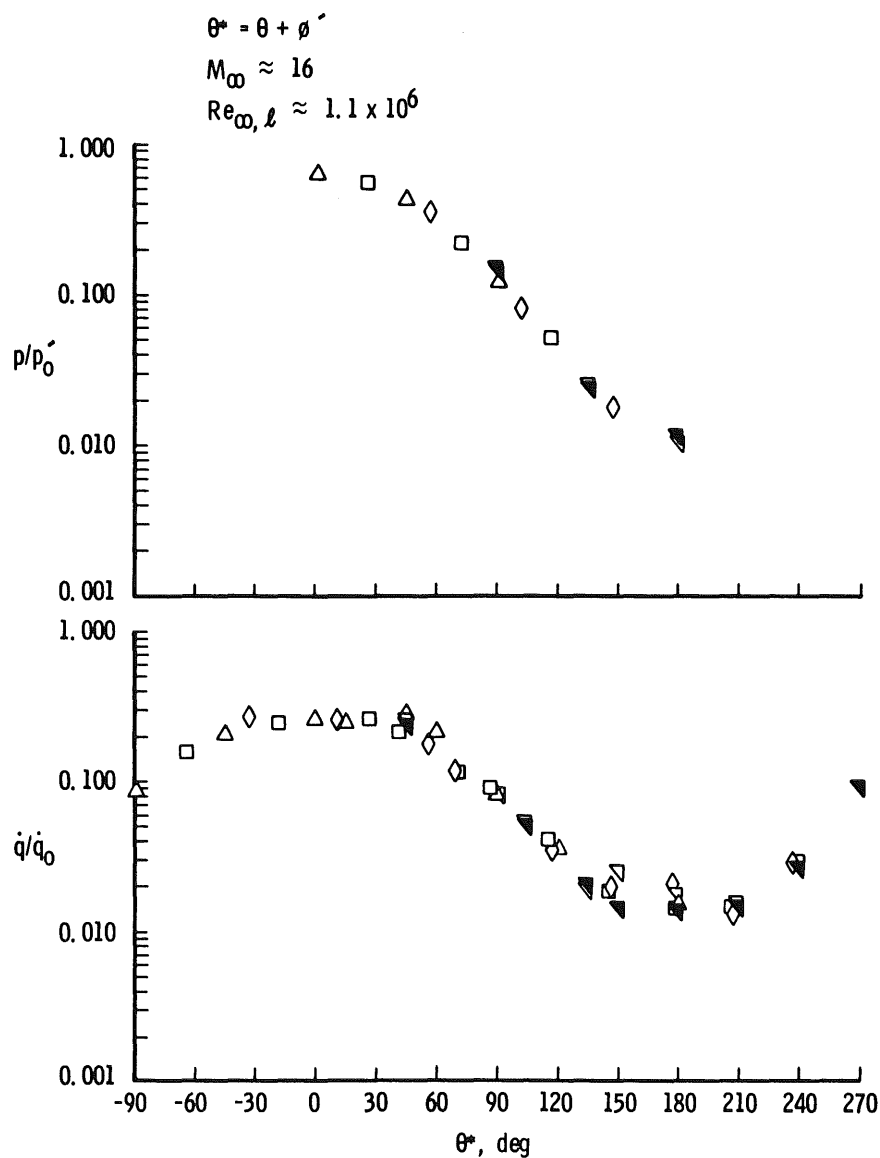


Figure 10. External tank peripheral heat-transfer and pressure distributions for  $\alpha' = 0$ .

Sym	Run	$\phi'$ , deg
$\triangle$	4832	0
$\square$	4849	$26^\circ 34'$
$\diamond$	4848	$56^\circ 19'$
$\nabla$	4875	90
$\blacktriangledown$	4881	90 (Clean Model)



a.  $x/\ell \approx 0.10$

Figure 11. External tank peripheral heat-transfer and pressure distributions for  $\alpha' = -30$  deg.

Sym	Run	$\theta^*$ , deg
$\triangle$	4832	0
$\square$	4849	$26^\circ 34'$
$\diamond$	4848	$56^\circ 19'$
$\nabla$	4875	90
$\blacktriangledown$	4881	90 (Clean Model)

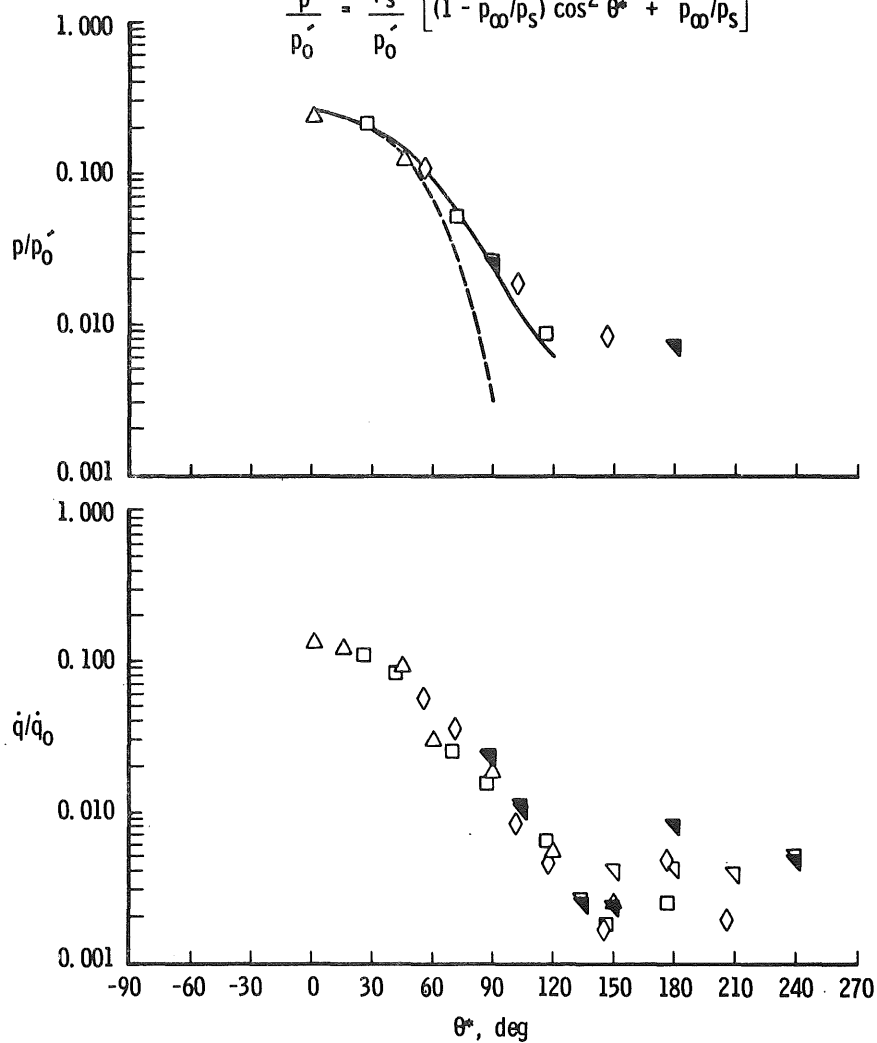
$$M_\infty \approx 16$$

$$Re_{\infty, \ell} \approx 1.1 \times 10^6$$

— Beckwith Experimental Distribution (Ref. 8)

--- Modified Newtonian:

$$\frac{p}{p_0} = \frac{p_s}{p_0} \left[ (1 - p_\infty/p_s) \cos^2 \theta^* + p_\infty/p_s \right]$$



b.  $x/\ell \approx 0.35$

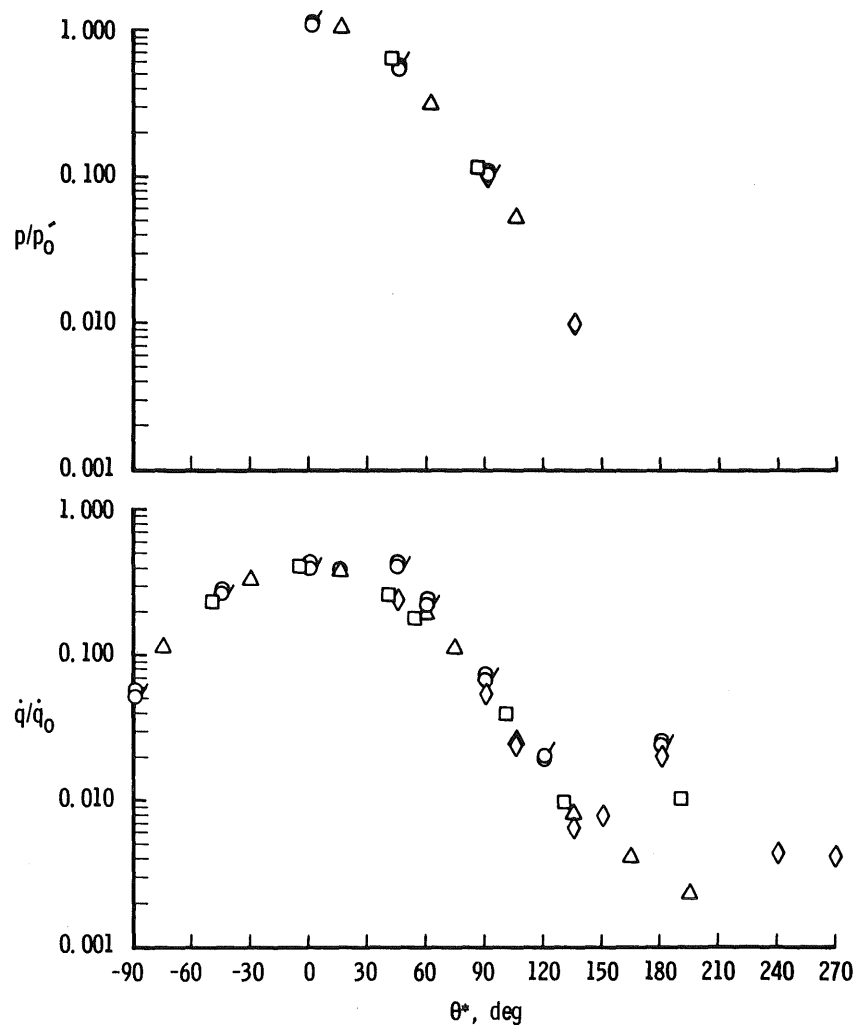
Figure 11. Concluded.

Sym	Run	$\phi'$ , deg
○	4833	0
△	4847	16° 6'
□	4846	40° 53'
◇	4845	90
○	4834	0 (Repeat Run)

$$\theta^* = \theta + \phi'$$

$$M_\infty \approx 16$$

$$Re_{\omega, l} \approx 1.1 \times 10^6$$



a.  $x/l \approx 0.10$

Figure 12. External tank peripheral heat-transfer and pressure distributions for  $\alpha' = -60$  deg.

Sym	Run	$\theta^*$ , deg
○	4833	0
△	4847	16° 6'
□	4846	40° 53'
◇	4845	90
♂	4834	0 (Repeat Run)

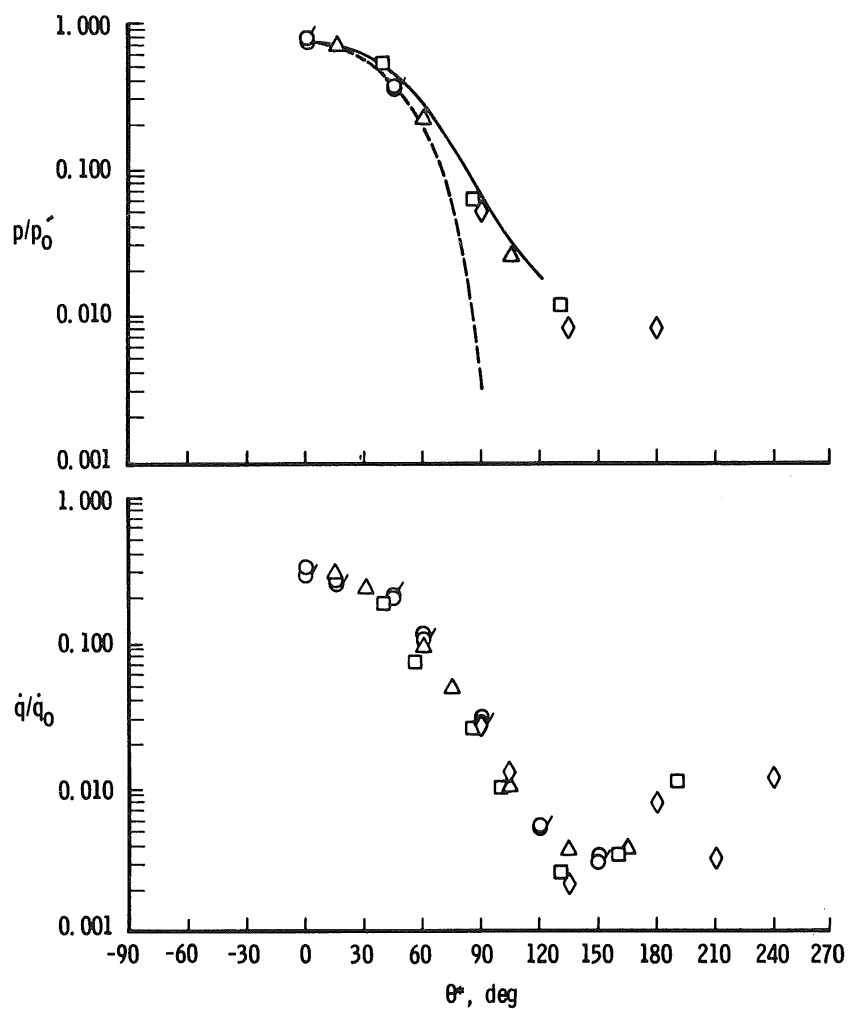
$$M_\infty \approx 16$$

$$Re_{\infty, \ell} \approx 1.1 \times 10^6$$

— Beckwith Experimental Distribution (Ref. 8)

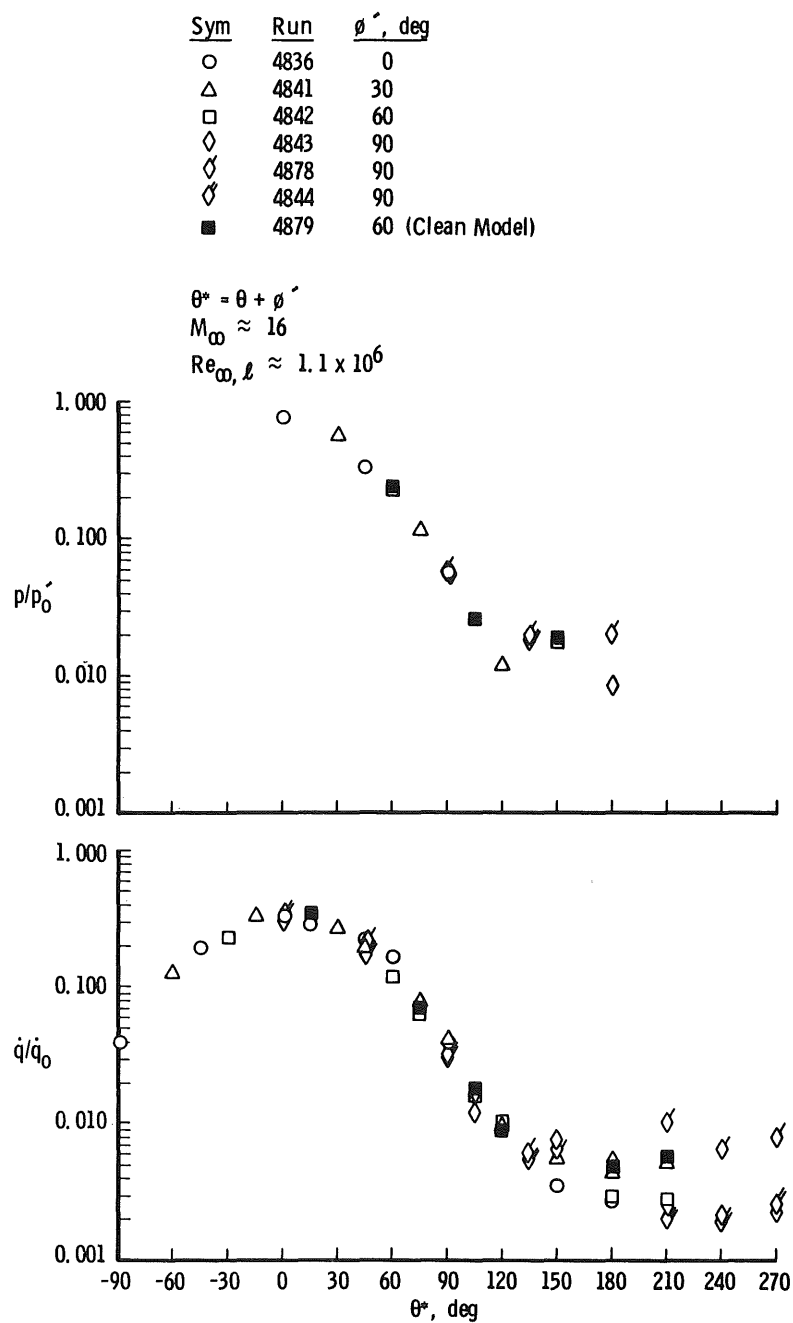
- - - Modified Newtonian:

$$\frac{p}{p_0} = \frac{p_s}{p_0} \left[ (1 - p_\infty/p_s) \cos^2 \theta^* + p_\infty/p_s \right]$$



b.  $x/\ell \approx 0.35$

Figure 12. Concluded.



a.  $x/\ell \approx 0.10$

Figure 13. External tank peripheral heat-transfer and pressure distributions for  $\alpha' = -90$  deg.

Sym	Run	$\theta^*$ , deg
○	4836	0
△	4841	30
□	4842	60
◇	4843	90
◇	4878	90
◆	4844	90 (Clean Model)
■	4879	60 (Clean Model)

$$M_\infty \approx 16$$

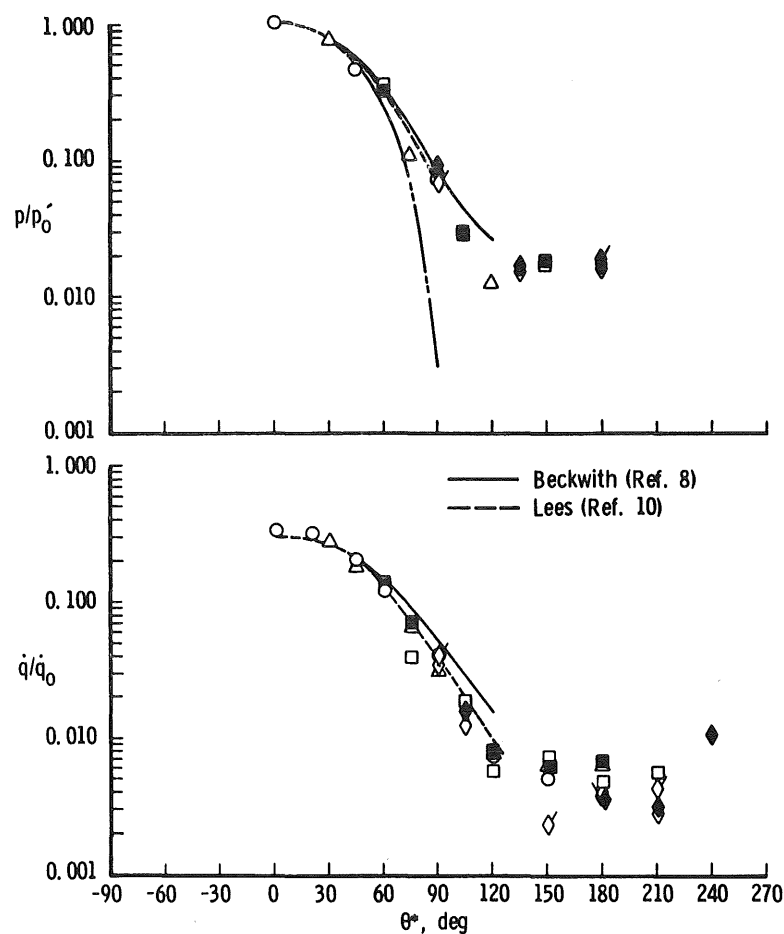
$$Re_{\infty, \ell} \approx 1.1 \times 10^6$$

— Beckwith (Ref. 8)

- - - Hamaker (Ref. 12)

— Modified Newtonian:

$$\frac{p}{p_0} = \frac{p_s}{p_0} \left[ (1 - p_\infty/p_s) \cos^2 \theta^* + p_\infty/p_s \right]$$



b.  $x/\ell \approx 0.35$

Figure 13. Continued.



Sym	Run	$\theta^\circ$ , deg
○	4836	0
△	4841	30
□	4842	60
◇	4843	90
◇	4878	90
◆	4844	90 (Clean Model)
■	4879	60 (Clean Model)

$$M_\infty \approx 16$$

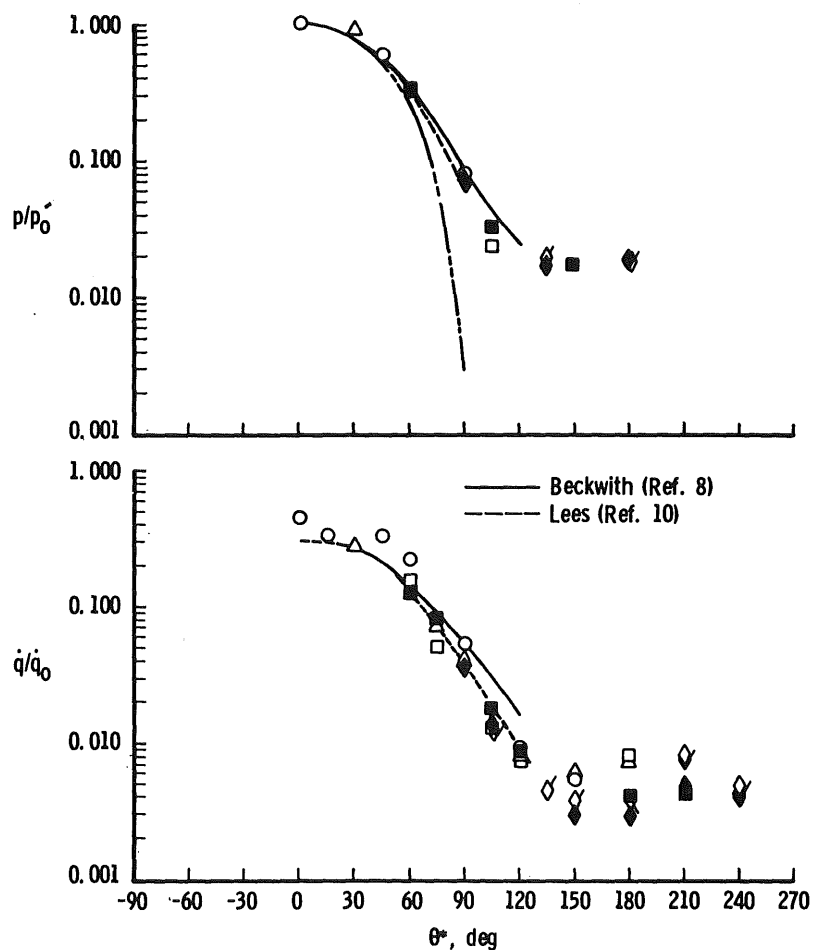
$$Re_{\infty, \ell} \approx 1.1 \times 10^6$$

— Beckwith (Ref. 8)

--- Hamaker (Ref. 12)

— Modified Newtonian:

$$\frac{p}{p_0} = \frac{p_s}{p_0} \left[ (1 - p_\infty/p_s) \cos^2 \theta + p_\infty/p_s \right]$$



c.  $x/\ell \approx 0.75$

Figure 13. Concluded.

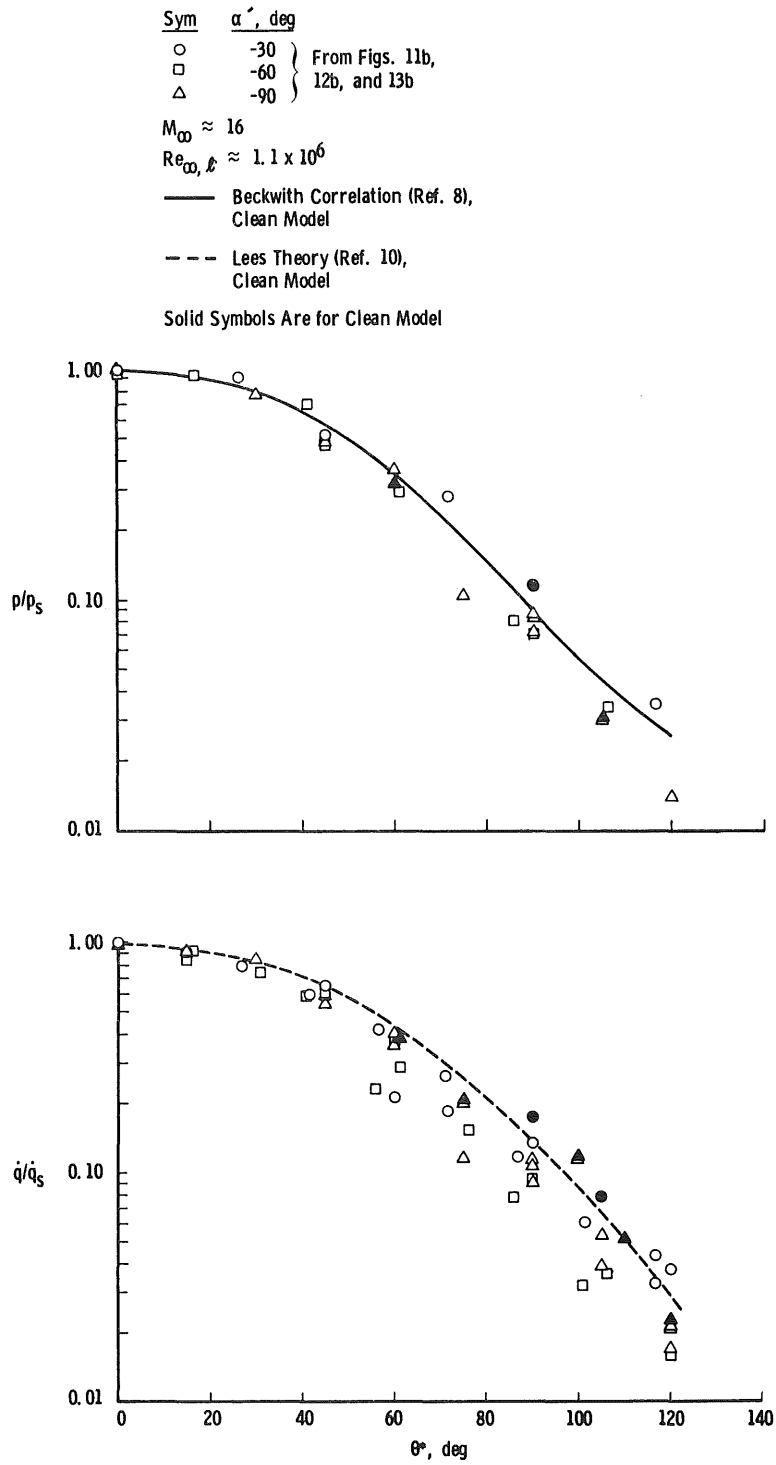
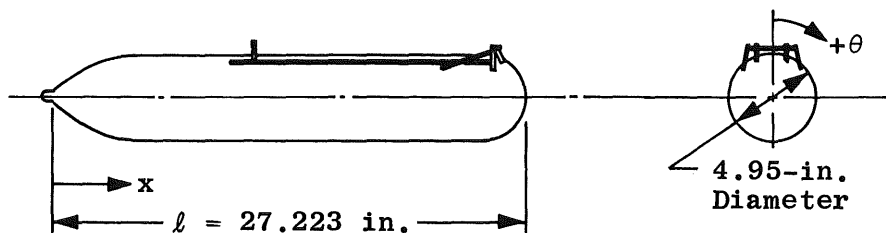


Figure 14. Heat-transfer and pressure peripheral distributions normalized to stagnation line values for  $\alpha' = -30, -60$ , and  $-90$  deg at  $x/\ell = 0.35$ .

### Table 1. Gage Locations



Heat Gage	$x/l$	$\theta$ , deg	Heat Gage	$x/l$	$\theta$ , deg
Q1	-0.0176	0	Q34	0.7557	60
Q2	0.0148	0	Q35	0.7493	90
Q3	0.0347	0	Q36	0.7557	120
Q4	0.0347	180	Q37	0.7557	150
Q5	0.0643	0	Q38	0.8659	0
Q6	0.1046	0	Q39	0.9192	0
Q7	0.1046	15	Q40	0.9577	0
Q8	0.1046	45	Q41	0.9822	0
Q9	0.1046	60	Q42	1.000	0
Q10	0.1046	90			
Q11	0.1046	120			
Q12	0.1046	150	Pressure Gage	$x/l$	$\theta$ , deg
Q13	0.1046	180			
Q14	0.1046	-90	P1	0	0
Q15	0.1046	-45	P2	0.0267	0
Q16	0.1612	0	P3	0.0515	0
Q17	0.1903	0	P4	0.0909	0
Q18	0.2140	0	P5	0.0909	45
Q19	0.2746	0	P6	0.0909	90
Q20	0.3437	0	P7	0.1375	0
Q21	0.3502	15	P8	0.2250	0
Q22	0.3437	45	P9	0.2415	0
Q23	0.3502	60	P10	0.3566	0
Q24	0.3437	90	P10A	0.3566	0
Q25	0.3502	120	P11	0.3566	45
Q26	0.3502	150	P12	0.3566	90
Q20A, 20A	0.3817	0	P13	0.6001	0
Q27	0.4196	0	P13A	0.6001	0
Q27A, 27A	0.4446	0	P14	0.7621	0
Q28	0.4696	0	P14A	0.7621	0
Q29	0.5350	0	P15	0.7621	45
Q30	0.6754	0	P16	0.7621	90
Q31	0.7493	0	P17	0.9283	0
Q32	0.7557	15	P18	0.9669	0
Q33	0.7493	45			

Table 2. Summary of Model Instrumentation  
a. Heat Gage Type\*

Gage	Runs			
	4831-4850	4851	4852, 4853	4874-4883
Q1	Coax	Coax	Coax	Coax-P
Q2	↓	Coax	Coax	↓
Q3	↓	Coax-P	Coax-P	↓
Q4	RT	RT	RT	RT
Q5	Coax	Coax-P	Coax-P	Coax-P
Q6	↓	↓	↓	RT
Q7	↓	↓	↓	↓
Q8	↓	Coax	Coax	↓
Q9	Coax-P	Coax-P	Coax-P	↓
Q10	Coax-P	Coax-P	Coax-P	↓
Q11	RT	RT	RT	↓
Q12	↓	↓	↓	↓
Q13	↓	↓	↓	↓
Q14	↓	↓	↓	↓
Q15	Coax	Coax-P	Coax-P	Coax-P
Q16	↓	Coax-P	Coax	Coax-P
Q17	↓	Coax	↓	RT
Q18	↓	↓	↓	↓
Q19	↓	↓	↓	↓
Q20	Coax-P	Coax-P	Coax-P	↓
Q20A	Coax	Coax	Coax	↓
Q21	Coax-P	Coax	Coax	↓
Q22	↓	Coax-P	Coax-P	↓
Q23	↓	Coax-P	Coax-P	↓
Q24	RT	RT	RT	↓
Q25	↓	↓	↓	↓
Q26	↓	↓	↓	↓
Q27	Coax-P	Coax	Coax	↓
Q27A	Coax	Coax	Coax	↓
Q28	Coax-P	Coax-P	Coax-P	↓
Q29	↓	↓	↓	↓
Q30	↓	↓	↓	↓
Q31	↓	↓	↓	↓
Q32	↓	↓	↓	↓
Q33	↓	↓	↓	↓
Q34	↓	↓	↓	↓
Q35	↓	↓	↓	↓
Q36	RT	RT	RT	↓
Q37	RT	RT	RT	↓
Q38	Coax-P	Coax-P	Coax-P	↓
Q39	↓	Coax	Coax	↓
Q40	↓	↓	Coax	↓
Q41	↓	↓	Coax-P	↓
Q42	↓	Coax-P	Coax-P	Coax-P

\*Coax - Coaxial Surface Thermocouple Gage  
 Coax-P - Coaxial Surface Thermocouple Gage  
 with Preamplifier  
 RT - Slug Calorimeter (Resistance Thermometer)

Table 2. Concluded  
b. Pressure Gage Type\*\*

Gage	Runs		
	4831-4842	4843-4853	4874-4883
P1	Strain Gage ↓	Strain Gage	Strain Gage
P2		↓	Var. Rel.
P3		↓	Strain Gage
P4		↓	Strain Gage
P5		↓	Var. Rel.
P6		Var. Rel.	Var. Rel.
P7		Strain Gage	Strain Gage
P8		↓	Var. Rel.
P9		↓	↓
P10		↓	Strain Gage
P10A		↓	Var. Rel.
P11		Var. Rel.	↓
P12		Strain Gage	↓
P13		↓	Strain Gage
P13A		↓	Var. Rel.
P14		↓	Strain Gage
P14A		↓	Var. Rel.
P15		Var. Rel.	Var. Rel.
P16		Strain Gage	Strain Gage
P17		Strain Gage	Strain Gage
P18		Strain Gage	Strain Gage

\*\*Strain Gage or Variable Reluctance Gage (Var. Rel.)

c. Heat Gage Specifications

Gage Type	Design Range, Btu/ft <sup>2</sup> -sec	Measured Heat-Transfer Rate, Btu/ft <sup>2</sup> -sec	Absolute Level Uncertainty, percent	Uncertainty in $\dot{q}/\dot{q}_0$ , percent
Coax	5-300	2-5 5-300	±15 ±9	±16 ±10
Coax-P	2-300	<0.6 0.6-2 2-300	±20 ±15 ±9	±21 ±16 ±10
RT	0.5-25	0.01-0.1 0.1-0.5 0.5-25	±20 ±15 ±9	±21 ±16 ±10

d. Pressure Gage Specifications

Gage Type	Design Range, psia	Measured Pressure, psia	Absolute Level Uncertainty, percent	Uncertainty in $\dot{p}/\dot{p}_0$ , percent
Strain Gage	0.01-2.0	0.002-0.01 0.01-0.1 0.1-2.0	±18 ±10 ±5	±19 ±11 ±6
Var. Rel.	0.001-0.1	0.001-0.01 0.01-0.15 >0.15	±15 ±5 ±10	±16 ±6 ±11

Table 3. Test Summary

$\alpha'$	$\phi'$	$\alpha_s$	$\psi_s$	$\phi$	$Re_{\infty, \ell}$ ( $10^{-6}$ )	$M_{\infty}$	Paint Data	Model Configuration	Run No.
0	0	0	0	0	1.03	15.53	Yes	With Structures*	4874
0	0	0	0	0	1.01	15.26	Yes	Clean Model**	4880
-30	0	-30	0	0	0.45	15.68	Yes	With Structures*	4831
-30	0	-30	0	0	1.02	15.68	↓	↓	4832
-30	26°34'	-26°34'	14°29'	0	0.91	15.50	↓	↓	4849
-30	56°19'	-16°06'	25°40'	0	1.00	15.51	↓	↓	4848
-30	90	0	30	0	1.02	15.53	↓	↓	4875
-30	90	0	30	0	0.99	15.89	↓	Clean Model**	4881
-60	0	-60	0	0	1.01	15.56	No	With Structures*	4833
-60	0	-60	0	0	1.03	15.88	↓	↓	4834
-60	0	-60	0	0	0.41	15.57	↓	↓	4835
-60	16°6'	-56°19'	25°40'	0	1.11	15.66	↓	↓	4847
-60	40°53'	-40°53'	48°35'	0	1.00	15.57	↓	↓	4846
-60	90	-60	0	0	1.04	15.70	↓	↓	4845
-90	0	-90	0	0	1.04	15.81	No	With Structures*	4836
-90	0	-90	0	0	0.39	15.34	↓	↓	4837
-90	30	-90	0	30	1.00	15.78	↓	↓	4841
-90	60	-90	0	60	1.02	15.75	↓	↓	4842
-90	60	-90	0	60	0.43	15.70	↓	Clean Model**	4879
-90	90	-90	0	90	1.03	15.66	↓	With Structures*	4843
-90	90	-90	0	90	1.02	15.86	↓	With Structures	4878
-90	90	-90	0	90	1.04	15.87	↓	Clean Body***	4844
-120	0	-120	0	0	1.02	16.07	No	With Structures*	4838
-120	0	-120	0	0	0.38	15.44	No	↓	4839
-120	16°6'	-123°41'	-25°40'	0	1.03	15.66	Yes	↓	4852
-120	40°53'	-139°07'	-48°35'	0	0.92	15.44	No	↓	4853
-150	0	-150	0	0	1.01	15.71	Yes	With Structures*	4840
-150	26°34'	-153°26'	-14°29'	0	0.84	15.33	↓	↓	4851
-150	56°19'	-163°54'	-25°40'	0	0.91	15.06	↓	↓	4850
-150	90	-180	-30	0	1.01	15.69	↓	↓	4877
-150	90	-180	-30	0	1.00	15.56	↓	Clean Model**	4883
-180	0	-180	0	0	1.03	15.50	Yes	With Structures*	4876
-180	0	-180	0	0	0.96	15.39	Yes	Clean Model**	4882

\* External tank with various attachment structures, fuel lines, service pipes, and wire tunnels.

\*\* All external structures, etc. removed from model.

\*\*\* All external structures, etc., removed from the model with the exception of the service pipes on the ogive nose section.

Table 4. Summary of Tunnel Conditions

Run	Time, msec	$p_{\infty}$ , psia	$\rho_{\infty}$ , lbm/ft <sup>3</sup> $\times 10^4$	$T_{\infty}$ , °R	$V_{\infty}$ , ft/sec	$M_{\infty}$	$q_{\infty}$ , psia	$Re_{\infty}/ft$ $\times 10^{-6}$	$Re_{\infty}, l$ $\times 10^{-6}$	$p_o$ , psia	$T_o$ , °R	$H_o$ , Btu/lbm	$\dot{q}_o$ , Btu/ft <sup>2</sup> -sec <sup>2</sup>	$St_o$	$p'_o$ , psia
4831	110	0.00225	0.620	94.6	7603	15.68	0.386	0.199	0.451	2654	4164	1178	46.60	0.095	0.720
4832	78	0.00518	1.42	95.5	7641	15.68	0.892	0.452	1.024	5925	4165	1190	71.68	0.063	1.661
4833	74	0.00562	1.45	101.2	7806	15.56	0.952	0.445	1.010	6225	4330	1242	78.18	0.062	1.774
4834	82	0.00467	1.36	89.4	7487	15.88	0.824	0.455	1.032	5715	4013	1142	65.40	0.064	1.534
4835	92	0.00253	0.606	109.1	8111	15.57	0.430	0.179	0.407	3038	4681	1341	57.79	0.097	0.801
4836	72	0.00509	1.41	94.1	7650	15.81	0.891	0.457	1.037	6157	4171	1192	71.81	0.063	1.659
4837	87	0.00275	0.606	118.6	8331	15.34	0.454	0.170	0.385	3070	4919	1416	63.53	0.098	0.846
4838	88	0.00412	1.28	83.8	7338	16.07	0.745	0.448	1.016	5399	3869	1096	59.07	0.065	1.387
4839	90	0.00265	0.593	116.7	8317	15.44	0.442	0.169	0.382	3084	4902	1410	62.45	0.099	0.825
4840	78	0.00510	1.40	95.3	7649	15.71	0.881	0.446	1.012	5916	4173	1192	71.41	0.063	1.640
4841	87	0.00462	1.34	90.4	7477	15.78	0.805	0.441	1.000	5427	4007	1139	64.47	0.064	1.499
4842	77	0.00503	1.40	94.1	7618	15.75	0.874	0.451	1.022	5921	4142	1182	70.39	0.063	1.627
4843	77	0.00520	1.43	95.2	7617	15.66	0.892	0.455	1.032	5871	4142	1182	71.12	0.062	1.661
4844	79	0.00494	1.40	92.4	7610	15.87	0.871	0.458	1.039	6108	4130	1179	70.08	0.063	1.623
4845	67	0.00550	1.46	98.7	7778	15.70	0.950	0.457	1.037	6441	4297	1233	77.32	0.062	1.769
4846	72	0.00542	1.42	99.6	7746	15.57	0.920	0.441	1.000	5989	4271	1223	75.34	0.063	1.713
4847	68	0.00567	1.54	96.1	7652	15.66	0.972	0.489	1.109	6393	4171	1193	75.12	0.060	1.811
4848	70	0.00574	1.46	103.0	7848	15.51	0.967	0.442	1.003	6248	4373	1256	79.86	0.062	1.802
4849	73	0.00554	1.34	107.6	8017	15.50	0.931	0.399	0.905	6154	4549	1310	82.65	0.065	1.735
4850	79	0.00551	1.37	105.0	7699	15.06	0.876	0.400	0.908	4892	4241	1210	72.53	0.064	1.631
4851	65	0.00582	1.31	116.4	8246	15.33	0.958	0.369	0.837	6191	4793	1387	89.97	0.067	1.785
4852	78	0.00532	1.43	96.9	7689	15.66	0.914	0.453	1.028	6074	4212	1205	73.70	0.062	1.702
4853	73	0.0056	1.37	107.0	7965	15.44	0.934	0.405	0.919	6025	4497	1293	81.47	0.065	1.741
4874	79	0.00571	1.48	101.0	7780	15.53	0.965	0.454	1.030	6219	4304	1234	78.03	0.062	1.797
4875	84	0.00529	1.43	96.6	7613	15.53	0.893	0.449	1.018	5661	4141	1181	71.08	0.062	1.663
4876	74	0.00577	1.48	101.7	7794	15.50	0.971	0.453	1.027	6218	4318	1238	78.63	0.062	1.808
4877	89	0.00507	1.40	94.9	7623	15.69	0.875	0.447	1.014	5830	4148	1184	70.56	0.063	1.629
4878	91	0.00449	1.34	87.6	7402	15.86	0.790	0.450	1.021	5408	3933	1116	62.22	0.064	1.470
4879	110	0.00232	0.61	99.4	7802	15.70	0.400	0.191	0.433	2829	4362	1240	50.59	0.096	0.745
4880	65	0.00668	1.56	112.0	8056	15.26	1.090	0.446	1.012	6688	4587	1324	90.60	0.061	2.032
4881	90	0.00458	1.31	91.0	7563	15.89	0.809	0.434	0.985	5700	4088	1165	66.48	0.065	1.507
4882	70	0.00591	1.43	107.7	7968	15.39	0.980	0.422	0.957	6221	4498	1295	83.55	0.063	1.827
4883	90	0.00511	1.39	95.7	7590	15.56	0.866	0.440	0.999	5529	4120	1174	69.49	0.063	1.613

## NOMENCLATURE

$H_o$	Test gas stagnation enthalpy, Btu/lbm
$H_w$	Test gas enthalpy at model wall temperature (540°R), Btu/lbm
$\ell$	Length of external tank model, in., see Fig. 5
$M_\infty$	Free-stream Mach number
P1, 2, etc.	Model pressure gage location and identification, see Tables 1 and 2
$p$	Model surface pressure, psia
$p_o$	Reservoir pressure, psia
$p_o'$	Total pressure behind normal shock in free-stream, psia
$p_s$	Measured stagnation line pressure, determined from Figs. 11b, 12b, and 13b at $\theta^* = 0$ , psia
$p_\infty$	Free-stream static pressure, psia
Q1, 2, etc.	Model heat-transfer-rate gage location and identification, see Tables 1 and 2
$\dot{q}$	Model surface heat-transfer rate, Btu/ft <sup>2</sup> -sec
$\dot{q}_o$	Stagnation heat-transfer rate on 1.0-in.-diam-hemisphere probe, Btu/ft <sup>2</sup> -sec
$\dot{q}_s$	Measured stagnation line heat-transfer rate, determined from Figs. 11b, 12b, and 13b at $\theta^* = 0$ , Btu/ft <sup>2</sup> -sec
$q_\infty$	Free-stream dynamic pressure, psia
$Re_\infty/ft$	Free-stream unit Reynolds number, ft <sup>-1</sup>
$Re_{\infty,D}$	Reynolds number based on free-stream conditions and model diameter
$Re_{\infty,\ell}$	Reynolds number based on free-stream conditions and model length
$St_o$	Stanton number based on $\dot{q}_o$ , $\dot{q}_o/\rho_\infty V_\infty (H_o - H_w)$
$T_o$	Reservoir temperature, °R
$T_\infty$	Free-stream static temperature, °R



$t$ , TIME	Time during the run at which the data are recorded, msec
$V_{\infty}$	Free-stream velocity, ft/sec
$x$	Longitudinal distance along model axis measured from ogive nose, in., see Fig. 5
$\alpha'$	Model total or complex angle of attack, $\cos^{-1} (\cos \alpha_s \cos \psi_s)$ , deg
$\alpha_s$	Sting angle of attack, deg
$\theta$	Gage location relative to model's vertical centerline, deg, see Fig. 5
$\theta^*$	Angular distance around cylinder from stagnation line in a plane normal to cylinder axis ( $\theta^* = \theta + \phi'$ ), deg
$\rho_{\infty}$	Free-stream density, lbm/ft <sup>3</sup>
$\phi$	Angle of roll, deg
$\phi'$	Aerodynamic roll angle based on pitch-yaw-roll sequence, $\phi' = \tan^{-1} [(-\cos \alpha_s \sin \psi_s \cos \phi + \sin \alpha_s \sin \phi) / (\cos \alpha_s \sin \phi \sin \psi_s + \sin \alpha_s \cos \phi)]$
$\psi_s$	Sting yaw angle, deg